**TECHNISCHE
UNIVERSITÄT
WIEN**

**VIENNA
UNIVERSITY OF
TECHNOLOGY**

D I P L O M A R B E I T

A Dual-Species Two-MOT Setup for Preparing a Bose-Fermi Mixture on an Atom Chip

Ausgeführt am

Atominstitut der österreichischen Universitäten,

Technischen Universität Wien

unter der Anleitung von

Univ.Prof. Dipl.-Ing. Dr. Jörg Schmiedmayer

durch

Maximilian Kuhnert

Schöffelgasse 12/6/3
A-1180 Wien

14.05.2008

Contents

List of Figures

Acknowledgments - Danksagungen

At first, I would like to thank my supervising tutor Dr. David A. Smith for his great support and advice during the whole year of my diploma work. I am particularly grateful for his great efforts to translate my thesis from technical English into proper English.

Bei Professor Jörg Schmiedmayer möchte ich mich speziell dafür bedanken, daß er mein Interesse an ultrakalten Atomen geweckt hat und mir die Gelegenheit gegeben hat, in seiner Arbeitsgruppe mitzuarbeiten. Ihm und seiner gesamten Arbeitsgruppe danke ich für das ausgezeichnete Betriebsklima und für das nahrhafte und ausgiebige gemeinsame Frühstück frühmorgens jeden Mittwoch.

Großer Dank geht an meine zwei betreuenden Dissertanten, Martin ('na is doch gut', eine kurze Einführung ins Schwäbische) Göbel und Christoph ('bitte vom Patienten zurücktreten' und erfahrenem Tankstellenkenner) Graf vom Hagen, für die zahlreichen Erklärungen, für ihre Geduld, für die Unterstützung beim Vertrautmachen mit dem Experiment und für den gemeinsamen Kampf an allen Fronten. Martin danke ich weiters dafür, daß er uns trotz dem Wechsel zu einem anderen Experiment weiterhin mit Rat und Tat zur Seite stand und Christoph für die aufopfernde Hingabe an das Experiment, trotz anderer Prioritäten. Zusammen mit Stephan ('Darum nerven Österreicher') Schneider haben sie ihr Herzblut in den Aufbau dieses Experiments gesteckt.

Besonderer Dank geht auch an meine immer fröhliche Diplomarbeitskollegin Barbara Stix (die mir gezeigt hat, wie leicht es ist, einen Schweinsbraten richtig zuzubereiten und einen Milchreis zu verderben, meine Schuld, ich geb es zu) , für die besonders gute Zusammenarbeit und ihre große Hilfsbereitschaft.

Auch Christian (der Mann mit der Lade der irdischen Genüsse und dem Whiskykreuz) Koller soll nicht unerwähnt bleiben. Er stand uns, dem Fermionen Team, in unseren schwersten

Abstract

A dual-species two-MOT setup for preparing a $^{87}Rb-^{40}K$ Bose-Fermi mixture on an atom chip is presented. The experimental system, consisting of a laser system and a two-chamber vacuum apparatus, where a collection MOT feeds a mirror MOT via a push laser beam (through a differential pumping stage), is illustrated in detail. Two of the eventual aims of the experiment are to investigate collapse phenomena in 1D and 3D Bose-Fermi mixtures and to study the thermalization of Bose-Fermi mixtures.

This diploma thesis was particularly focused on the following tasks:

- the characterisation and construction of the magnetic bias field coils setup and its implementation into the experiment

- the characterisation and optimisation of a single ^{87}Rb and a single ^{40}K MOT in the collection chamber and the testing of the home-built enriched potassium dispensers

- (very carefully) inserting the atom chip and its ∼40kg mounting into the science chamber and subsequently, connecting the collection chamber with the science chamber

- the setup and implementation of the MOT and push beam optics (and the optics board assembly) around the vacuum system

- the reestablishment of the rubidium and potassium collection MOTs

- establishing the first ^{87}Rb mirror MOT in the science chamber

- realising the loading of atoms from the collection MOT to the mirror MOT via a push beam.

Chapter 1

Introduction

The effect of Bose-Einstein condensation was predicted theoretically in 1925 [1, 2], but the experimental realisation took until 1995 [3]. In 2001, the Nobel prize was awarded to Cornell, Wieman and Ketterle for the realisation and research of Bose-Einstein condensate (BEC). On the way towards a BEC, a variety of cooling and trapping mechanisms for neutral atoms were explored. For cooling atoms using laser light, Chu, Cohen-Tanoudji and Phillips received the Nobel prize in 1997. Since then, ultracold atoms have become a rapidly expanding area of research and the number of research groups working with atom traps worldwide is still increasing[1].

Up to now, BECs in most alkali metals have been realized and examined. Additionally, degenerate Fermi gases[2] (DFGs) have been produced with potassium (1999, [4]) and lithium (2001, [5]).

This thesis describes an experiment to study a Bose-Fermi mixture on an atom chip. In order to produce a DFG, the fermions will be sympathetically cooled with a bosonic interaction partner[3], as the Pauli exclusion principle prevents identical Fermions from interacting, making it impossible for them to thermalize. Sympathetic cooling was first proposed for two-component

---

[1]currently more then 150 groups woldwide are working with ultracold atoms, see http://www.uibk.ac.at/exphys/ultracold/atomtraps.html (accessed 01.05.08)

[2]A gas of fermionic particles, described by Fermi-Dirac statistics and obeying the Pauli exclusion principle. If the temperature of the gas is less than the Fermi temperature, the gas enters the degenerate regime where quantum statistical effects become significant [4].

[3]One could also use a two-component Fermi gas [6] .

plasmas [7].

In the following, the progress of an experiment using this approach to establish a DFG of fermionic ^{40}K using bosonic ^{87}Rb as a coolant is reported. The goals of this experiment are to study the thermalization of Bose-Fermi mixtures in 3D, 1D and in the 3D/1D crossover regime, and furthermore, to examine collapse phenomena in 1D and 3D mixtures, as ultracold ^{40}K and ^{87}Rb have a naturally attractive scattering interaction.

This diploma thesis was intended to emphasize the characterisation and optimisation of the two dual-species magneto-optical traps used in this experiment. Nonetheless, an exact characterisation of the mirror MOT was not possible, due to the inevitable delay, caused by repeatedly breaking vacuum windows.

This thesis is organized in the following way: Chapter 2 gives an overview of the theory of laser cooling and introduces the basic concepts of trapping and cooling neutral atoms in a magneto-optical trap. Chapter 3 details the experimental setup, consisting of the laser system, the vacuum assembly (housing the atom chip), the bias-field coils and the MOT optics setup. Chapter 4 focuses on the measurement and characterisation of the two single-species MOTs in the collection chamber. Chapter 5 presents the preliminary results of a ^{87}Rb mirror MOT in the science chamber and discusses the complexity of the optimisation process. Finally, chapter 6 reports on the progress of the experiment and the achievements, made during this diploma work.

Chapter 2

Theory

2.1 Laser Cooling

Laser cooling techniques rely on the interaction between light and matter. Photons can transfer momentum and thereby apply a force on atoms. How this interaction works and how it can be used to slow the atomic motion, and subsequently trap and cool atoms is discussed in the following chapter. The main idea of laser cooling goes back to the year 1975 with the publications of Hänsch and Schawlow [8] (optical molasses) and Wineland and Dehmelt [9].

2.1.1 The Scattering Force

Lasers produce well-collimated monochromatic[1] beams of light ($\hbar\vec{k}$), propagating in one direction, that can exert a force on an atom. Assuming now a two-level atom with a ground state $|g\rangle$ and an excited state $|e\rangle$, the energy difference between the two states shall be denoted as $h\nu$ and the lifetime of the excited state shall be referred to as τ, with a natural linewidth of $\Gamma = 1/\tau$. Each absorbed photon, with energy $h\nu_L$, transfers the momentum $\hbar\vec{k}$ to an atom and excites it. The atom falls back into the ground state by spontaneously emitting a photon into a random direction in 4π. Thus, the recoil momentum, associated with the spontaneous fluorescence, is in random direction, so its average over many emission events results in a zero

---

[1]Here monochromatic means that the linewidth of the laser is much less than the linewidth of the atomic transition.

net effect on the atomic momentum. The scattering of many photons gives an average force in the direction of $\vec{k}$. For dN absorbed photons, the average momentum transfer is $dp = \hbar\vec{k}dN$, resulting in the applied force [10]

$$\vec{F}_{scatt} = \frac{d\vec{p}}{dt} = \hbar\vec{k}\frac{dN}{dt} = \hbar\vec{k}R \tag{2.1}$$

with the scattering rate $R = \Gamma\rho_e$ and ρ_e the excited state population fraction ($\rho_e + \rho_g = 1$). This occupation probability ρ_e can be defined by solving the static optical Bloch equations (using the electric dipole and rotating wave approximations) [11, 12, 10], which leads to the following equation for the scattering force (also known as *spontaneous force* or *radiation pressure*)

$$\vec{F}_{scatt} = \hbar\vec{k}\cdot\frac{\Gamma}{2} \cdot \frac{I/I_{sat}}{1 + I/I_{sat} + 4\delta^2/\Gamma^2} \tag{2.2}$$

with the laser light intensity I and the on-resonance saturation intensity $I_{sat} = \pi hc/3\lambda^3\tau$. The frequency detuning from resonance $\delta = \omega_L - \omega_0$ equals the difference between the laser frequency ω_L and the atomic resonance frequency ω_0, for an atom at rest. For a moving atom, the additional detuning, caused by the Doppler shift $\delta_D = -\vec{k}\vec{v}$, [13] has to be taken into account.

As $I \to \infty$ the scattering force tends to a limiting value of [10]

$$F_{scatt}^{max} = \hbar k\frac{\Gamma}{2}, \tag{2.3}$$

as R tends to $\Gamma/2$ at high intensities, because the populations in the upper and lower levels both approach $1/2$ [10] for an atomic ensemble.

For an atom of mass m the scattering force produces a maximum acceleration of [10]

$$a_{max} = \frac{\hbar k}{m}\frac{\Gamma}{2} = \frac{v_r}{2\tau}, \tag{2.4}$$

with the recoil velocity $v_r = \hbar k/m$. For a ^{87}Rb atom, $a_{max} = 1.1 \cdot 10^5 m/s^2$ and for a ^{40}K atom $a_{max} = 2.52 \cdot 10^5 m/s^2$, being 10^4 times greater than the gravitational acceleration.

2.1.2   Optical Molasses

As atoms in a gas move in all directions, reducing their temperature requires laser cooling in all three cartesian directions. Therefore, let us now extend the above discussion by including the radiative force of two low-intensity laser beams of the same frequency, intensity, and polarization that counterpropagate relative to one another. The net force (eq. 2.5), found by adding the scattering forces (compare eq. 2.2) produced by each beam, obviously vanishes for atoms at rest. However, for a moving atom the Doppler effect leads to an imbalance in the forces [10].

$$\vec{F}_{scatt}^{tot} = \vec{F}_{scatt}\left(\vec{k}\right) + \vec{F}_{scatt}\left(-\vec{k}\right) = \hbar\vec{k}\cdot\frac{\Gamma}{2}\cdot\left(\frac{I/I_{sat}}{1 + I/I_{sat} + \frac{4\left(\delta - \vec{k}\vec{v}\right)^2}{\Gamma^2}} - \frac{I/I_{sat}}{1 + I/I_{sat} + \frac{4\left(\delta + \vec{k}\vec{v}\right)^2}{\Gamma^2}}\right)$$
$$(2.5)$$

If the laser is tuned below atomic resonance (red detuned), the frequency of the light in the beam opposing the atomic motion is Doppler shifted toward the blue in the atomic rest frame, and is therefore closer to resonance. The contrary holds for the other beam, which is shifted further away from resonance. Atoms will therefore interact more strongly with the laser beam that opposes their velocity and they will be decelerated.

A series expansion for small velocities $kv \ll \Gamma$ and low intensities $I/I_{sat} \ll 1$ gives [10]

$$\vec{F}_{molasses} \simeq 8\hbar k^2 \frac{I}{I_{sat}}\cdot\frac{\delta\vec{v}}{\Gamma\left(1 + 4\delta^2/\Gamma^2\right)^2} = -\alpha\vec{v}. \qquad (2.6)$$

with the damping coefficient α. For $\delta < 0$, this force opposes the velocity and therefore viscously damps the atomic motion and forms so-called *optical molasses* (compare with Fig. 2.1). However, as there is no restoring force for atoms that have been displaced from the center of 3D optical molasses, it cannot be referred to as a trap for neutral atoms. The first 3D optical molasses was realized in 1985 in the Bell Laboratories [14], cooling sodium atoms to 240μK. The lifetime of the atoms in the trap was approximately 0.1s. In order to perform experiments it is desirable to contain the atoms for a much longer time than this. Somehow a spatially-dependent force has to be generated to trap the atoms (see section 2.2.1).
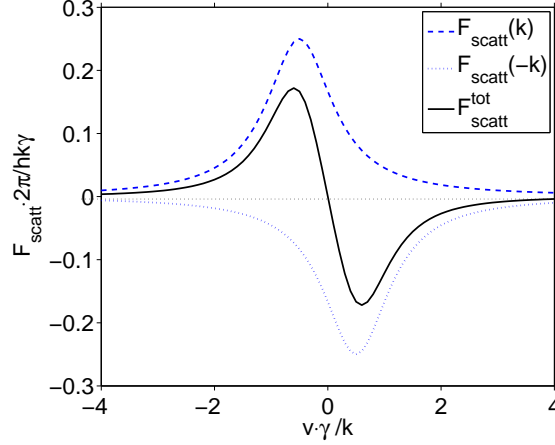
Figure 2.1: Dependence of 1D optical molasses damping forces on the atom velocity
The dashed and dotted traces show the force from each laser beam, and the solid curve gives the total force generated by the atom interaction with the both beams. In close proximity to zero velocity the net force is almost linear and mimics a viscous damping force. The traces have been calculated for $I = I_{sat}$ and a red detuning of $\delta = -\Gamma/2$.

2.1.3 The Doppler Cooling Limit

If there were no other influence on the atomic motion, all atoms would quickly decelerate to $v = 0$ and the sample would reach $T = 0$, but there is also some heating caused by the light beams. The spontaneous emission that always accompanies F_{scatt} causes the atom to recoil in random directions. These recoil kicks lead to a random walk in the velocity, analogous to the Brownian motion. As already discussed, the average momentum transfer of many spontaneous emissions is zero, but the mean square of the momentum is finite. Since the atomic momentum changes by $\hbar k$ for each spontaneous emission, their kinetic energy changes on average by at least the recoil energy $E_r = \hbar^2 k^2 / 2m$ and the atoms are heated.

The competition between this heating with the damping force results in a nonzero kinetic energy in steady state. The temperature found from the kinetic energy is called the Doppler temperature T_D [12].

$$T_D = \frac{\hbar\Gamma}{2k_B},$$

(2.7)

where k_B is the Boltzmann constant. This Doppler cooling limit depends only on the linewidth Γ of the atomic transition. For ^{87}Rb, the Doppler limit is given by $T_D = 146\mu$K [15] and for ^{40}K it is given by $T_D = 149$nK [16].

2.1.4 Sub-Doppler Cooling

Experimental measurements [17] found much lower temperatures under certain circumstances, in particular when the ambient magnetic field was compensated. The two-level model of an atom cannot explain this *sub-Doppler cooling*. Real alkali atoms have degenerate energy levels. Remarkably this does not just complicate the situation, but actually allows new cooling techniques. The new cooling mechanisms (*Sisyphus cooling*) are based on optical pumping, light shift and polarization gradients. Detailed descriptions are out of the scope of this introduction and may be found in [18] and [19].

2.1.5 Limits of Laser Cooling

The fundamental limit of laser cooling is given by the single-photon recoil energy E_{rec}.

$$E_{rec} = \frac{\hbar^2 k^2}{2m} = k_b T_{rec}$$

In the case of the D_2-line of ^{87}Rb, T_{rec} equals 362nK [15] and for ^{40}K $T_{rec} = 815$nK.

Techniques to circumvent this limit are known as *Raman cooling* [20] and *dark-state cooling* [12].

2.2 Trapping Neutral Atoms

In 3D optical molasses, cold atoms accumulate in the region where the three orthogonal pairs of laser beams intersect, because it takes a considerable time for atoms to move out. However, optical molasses cannot trap the atoms, as the dissipative force acting on the atoms is only velocity-dependent but not spatially-dependent. By applying a magnetic quadrupole field and using particular polarizations, a trap is formed. The next part will focus on these so-called *magneto-optical traps*.

Other possibilities for trapping neutrals atoms shall only be mentioned very briefly. These are *optical dipole traps*, relying on the dipole force applied by a gradient in the light-shift generated by strongly focused laser beam, and *magnetic traps*, based on the interaction between the nuclear magnetic moment μ and an external magnetic field. A more detailed description can be found in [12] and references therein.

2.2.1 Magneto-Optical Trap (MOT)
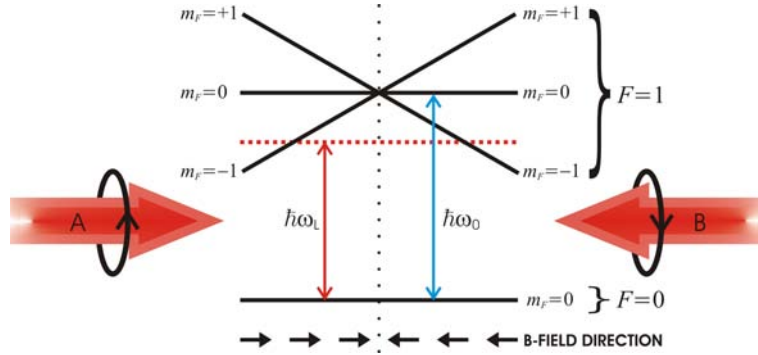
Figure 2.2: The mechanism of a magneto-optical-trap in 1D

Arrangement for a MOT in 1D. The dotted line resembles the laser frequency, which is red-detuned from resonance by δ for zero magnetic field. For $z > 0$ the σ^- (in respect to its $\vec{k}$ vector) light, propagating to the left, becomes resonant with the atomic transition $|F = 0, m_F = 0\rangle \rightarrow |F = 1, m_F = -1\rangle$, due to the Zeeman shift, caused by the inhomogeneous magnetic field $B = -B_0 z$. In contrast, the σ^- light propagating to the right is further away from resonance with the $|F = 1, m_F = +1\rangle$ hyperfine energy level. For $z < 0$ the laser beams act vice versa. Therefore, the atom is always pushed to $z = 0$, where the scattering forces of the two beams equalize, trapping the atom. Illustration taken with permission from [21].

The most widely used trap for neutral atoms is the magneto-optical trap (MOT), which was first demonstrated in 1986 [22] at Bell laboratories. The principal idea was suggested by Jean Dalibard and is illustrated in Fig. 2.2. For a simple two-level atom the $(2F + 1)$-degenerate magnetic hyperfine levels can be split by applying an inhomogeneous magnetic field, resulting in a ground state $|g, F = 0, m_F = 0\rangle$ and three excited states $|e, F' = 1, m_{F'} = 0, \pm 1\rangle$. In the one-dimensional case with a linearly inhomogeneous magnetic field $B(z) = -B_0 z$ (with a constant $B_0 > 0$) the energy levels are position-dependently Zeeman shifted by $\Delta E(z) =$
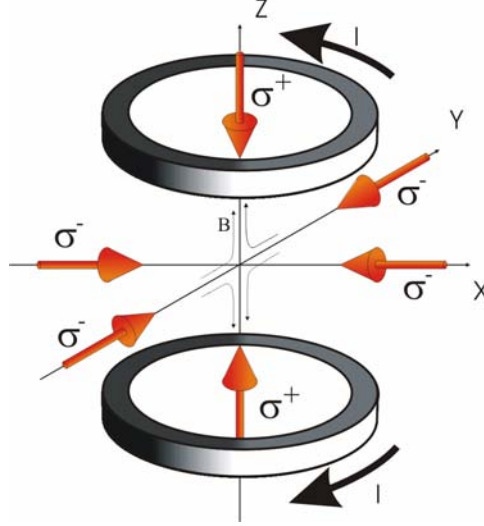
Figure 2.3: The mechanism of a magneto-optical-trap in 3D
Arrangement for a six-beam MOT in 3D. the quadrupole magnetic field is generated by two coils in anti-Helmholtz configuration. The six circularly-polarized laser beams intersect at the zero point of the magnetic field, trapping the atoms. The polarization are given in respect to the $\vec{k}$-vectors of the beams.

$g_f m_f \mu_B |B(z)|$, where g_f is the Landé factor and μ_B is the Bohr magneton. The resonance frequency is now position-dependent, and for $z \neq 0$, different for each the three excited energy levels. Furthermore, the transition to an excited state has become dependent on the beam polarization, σ^+ polarized light driving $\Delta m_F = +1$, σ^- driving $\Delta m_F = -1$ and π driving $\Delta m_F = 0$ transitions.

For two counter-propagating laser beams having opposite circular polarization and a frequency slightly less than the atomic resonance frequency for zero magnetic field, the Zeeman shift causes an imbalance in the scattering force. For $z \neq 0$, the $\Delta m_F = -1$ transition is shifted by the Zeeman effect closer to resonance. Therefore photons driving the σ^- transitions are preferably absorbed. In Fig. 2.2 both laser beams are chosen to be σ^- polarized in respect to the direction of propagation. For $z > 0$ the laser beam, titled as 'A', is pointing parallel to the magnetic field vector in the negative z direction, drives the desired σ^- transitions, whereas the counter-propagating laser beam, being antiparallel to the magnetic field vector, is driving σ^+ transitions and is therefore further away from resonance. A net scattering force that pushes

the atoms back into the trap center is obtained. A similar process occures for a displacement of the atom in the negative z direction, where now the laser beam coming from the left is driving σ^- transitions and thereby closer to resonance, than the second laser beam, pushing the atoms again back towards $z = 0$. Eq. 2.5 becomes

$$\vec{F}_{MOT}^{tot} = \hbar\vec{k}\cdot\frac{\Gamma}{2} \cdot \sum_{m_{F'}=-1}^{m_{F'}=1} \left(\frac{I/I_{sat}}{1 + I/I_{sat} + \frac{4\left(\delta - \delta_B - \vec{k}\vec{v}\right)^2}{\Gamma^2}} - \frac{I/I_{sat}}{1 + I/I_{sat} + \frac{4\left(-\delta_B + \vec{k}\vec{v}\right)^2}{\Gamma^2}} \right) \qquad (2.8)$$

with $\delta_B = \left(g_{F'}m_{F'} - g_F m_F\right)\mu_B \left|B\left(z\right)\right|/\hbar$.

This concept can be expanded into 3D system by adding two more pairs of counter-propagating laser beams and using a magnetic quadrupole field, compare Fig. 2.3. The quadrupole magnetic field can be generated by two coils in anti-Helmholtz configuration. Usually, weak magnetic fields (gradients at trap center of 15-20G/cm) are sufficient.

A brief discussion on the loading behaviour of a MOT can be found in section 4.2.3, together with experimental results.

MOTs are widely used to trap neutral atoms, because they are very robust traps as they [12]

- do not depend on very precise beam alignment, power balancing or a high degree of circular polarizations

- magnetic field gradients are modest and can be achieved with simple, air-cooled coils

- the trap is easy to construct as it can be operated with a room temperature vacuum apparatus, capturing alkali atoms from the vapour $(10^{-8}mbar)$

- low-cost diode laser system can be used to produce the light for all alkalis except Na and Li

Therefore, the MOT has become one of the least expensive ways to produce atomic samples with temperatures below 1mK.

Chapter 3

Experimental Setup

3.1   Introduction

The purpose of this chapter is to make the reader familiar with the setup and some technological details of the experiment. As describing every technological and experimental detail would be completely out of the scope of this diploma thesis, the following selection, of the most relevant experimental parts, had to be made. First, the laser system, providing the laser radiation for trapping and cooling the two atomic species, ^{87}Rb and ^{40}K, is presented. The second part describes the two-chamber vacuum system, consisting of a collection chamber with the atomic sources and a science chamber, where the atomchip is situated and a degenerate Bose-Fermi mixture will be produced. The never-ending problems that occured with the vacuum windows of the science chamber are discussed. The next part focuses on the external magnetic bias field coils, used together with the broad copper U wires to generate a magnetic quadrupole field for the science MOT. Finally, the installation of the collection and science MOT optics is explained .

3.2   Laser System

A brief introduction to laser cooling was presented in chapter 2.1. The purpose of this section is to explain how the laser radiation, required for cooling and trapping atoms, is generated. The

first part emphasizes the key requirements for the applied laser radiation. The experimental realization, for the two atomic species used in this experiment, is presented in the subsequent subsections. The different laser locking techniques used in this experiment are also explained. Finally, the setup of the optical table is illustrated.

3.2.1 Essential Features of the Laser System

The key requirements for the laser radiation, for laser cooling and trapping, are given below.

- **Frequency requirements:**

  - Narrow linewidth: The frequency linewidth of the applied radiation has to be smaller than the natural linewidth of the stimulated transition (see table 3.1).

  - Long-term stability: The frequency drift during many experimental cycle has to be much smaller than the natural linewidth of the transition.

  - Reproduceability: The frequency setting has to be reproducible not only for one, but for many experimental runs, in order to retrieve results that can be compared within each other.

- **Beam intensity:** In order to trap the maximum number of atoms the power of each trapping beam has to be larger than the saturation intensity of the relevant atomic species (compare table 3.1).

- **Tuneability:** Sweeping the laser frequency over several linewidths is often required during an experiment[1].

- **Ease of operation:** The less attention a laser system needs for stable operation during an experiment, the more likely the unperturbed operator may focus on nice, physically interesting results.

---

[1]as an example: for performing atom number determinations (see chapter 4.2.1)

Element	Transition	Lifetime	Linewidth	Reference
^{87}Rb	$5s_{1/2} - 5p_{3/2}$	26.24ns	$2\pi\times6.065(9)$MHz	[15]
^{40}K	$4s_{1/2} - 4p_{3/2}$	25.7ns	$2\pi\times6.2$MHz	[16]

Table 3.1: Natural Linewidth of the relevant transitions of ^{87}Rb and ^{40}K.

3.2.2 Rubidium Laser System

Rubidium Cooling Laser - FM lock

The setup of the rubidium cooling laser is depicted in Fig. 3.1. A commercial CW DPSS laser[2] emits 10W of laser power at a wavelength of 532nm. This laser beam is then converted by a Ti:sapphire ring laser system[3] into the desired wavelength of 780.24nm with a specified linewidth of 100kHz and a power output of approximately 1.6W. A small fraction of this output (approximately 5mW) is then directed, through an EOM[4], to an absorption spectroscopy assembly.

For frequency locking, a frequency-modulation (FM) lock is applied, which shall be briefly described below.

The laser frequency[5] is modulated[6] by an EOM in order to generate sidebands in the frequency spectrum. The modulated laser field $E(t)$ can be written as

$$E\left(t\right) = E_0 e^{i((\omega_0 t+\beta sin(\omega_m t))} \tag{3.1}$$

with the carrier frequency ω_0, the modulation depth β and the modulation frequency ω_m. Expanding this into Bessel functions yields [25]

$$E\left(t\right) = E_0 e^{i\omega_0 t} \sum_{n=-\infty}^{n=\infty} J_n\left(\beta\right) e^{in\omega_m t}, \tag{3.2}$$

where J_n is the nth-order Bessel function. For small modulation depths $\beta < 1$, sidebands

---

[2]CW DPSS = continuous-wave diode-pumped solid state; Verdi V18, Coherent, Inc.; a data sheet can be found at http://www.coherent.com/downloads/VerdiV18_DSrevB.pdf

[3]MBR (Monolithic Block Resonator) 110, Coherent, Inc.

[4]electro-optical modulator, using the electro-optical effect, see [24]

[5]Assuming the laser is operated in single-frequency mode and, furthermore, that the linewidth of this frequency is much smaller than the distance from the central line to the sidebands.

[6]in the case of diode lasers, the laser frequency may be easily modulated by modulating the laser current
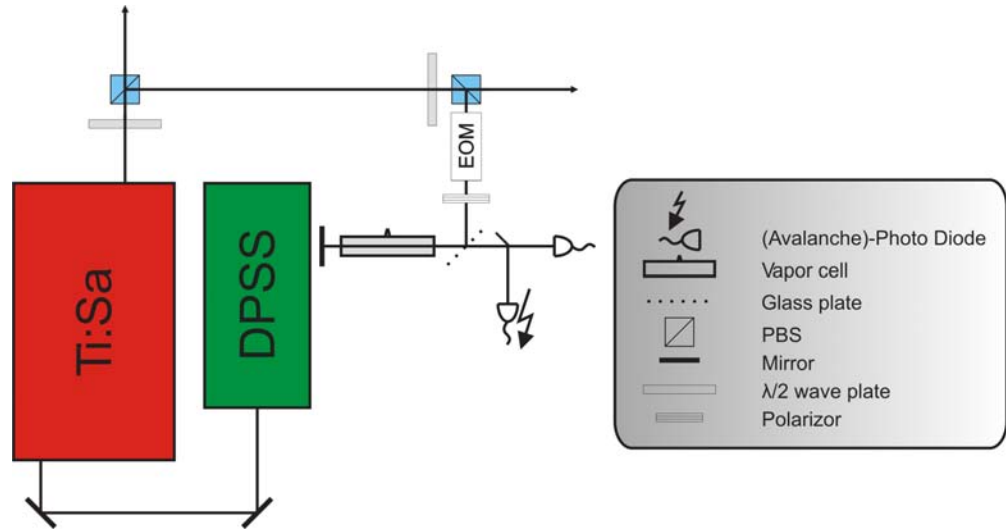
Figure 3.1: Rubidium cooling laser layout

After the EOM, a 4mm-thick glassplate generates two parallel beams which travel through a rubidium vapour cell. One beam is used for generating a standard absorption spectroscopy signal picked up by a standard photodiode. The second beam is directed to an avalanche photodiode and is used to generate the error signal. Diagram based on [23].

with $n > 1$ can be neglected, thus resulting in three frequencies: the carrier frequency (ω_0) and two sideband frequencies ($\omega_o \pm \omega_m$).

Bessel functions exhibit the following symmetry relation:

$$J_{-n}(\beta) = (-1)^n J_n(\beta) \tag{3.3}$$

which is, in our case,

$$J_{-1}(\beta) = -J_1(\beta). \tag{3.4}$$

and gives

$$E(t) \cong E_0 \left(J_1(\beta) e^{i(\omega_0 + \omega_m)t} + J_0(\beta) e^{i\omega_0 t} - J_{-1}(\beta) e^{i(\omega_0 - \omega_m)} \right). \tag{3.5}$$

Therefore, the carrier and the $n = 1$ sideband are in phase, but, in respect to these two, the $n = -1$ sideband is out of phase by 180°. Neglecting now the beating signal between the two sidebands, which is small and can be filtered, only the beating signal between carrier and each sideband is left. If there is no absorber, such as an atomic-vapour cell, in the beam path, the beating signal between carrier and lower sideband and the beating signal between carrier and upper sideband match exactly in amplitude and frequency (ω_m), but are exactly out of phase and hence cancel. Only in the case that there is an absorber in the beam path, changing amplitude and phase with respect to frequency, a non-zero beat signal can be detected. Using an atomic-vapour cell, the beat signal contains all information about absorption and dispersion of the light within this cell. This information may be retrieved from the beat signal using a phase detector.

Inserting a transfer function $T(\omega_n) = e^{-\delta_n - i\phi_n}$ in eq. 3.2, accounting for the absorber, where δ_n denotes field amplitude attenuation and ϕ_n the phase shift at frequency ω_n, one can thereby derive, as stated in [26], assuming that $|\delta_n - \delta_{n+1}| \ll 1$, $|\phi_n - \phi_{n+1}| \ll 1$, $\beta \ll 1$, $J_0(\beta) \approx 1$ and $J_1(\beta) \approx \beta/2$,

$$\left| E^2(t) \right| = E_0^2 e^{-2\delta_0} \left[1 + \beta(\delta_{-1} - \delta_1) \cos(\omega_n t) + \beta(\phi_{-1} + \phi_1 - 2\phi_0) \sin(\omega_n t) \right]. \tag{3.6}$$

In eq. 3.6 the absorption component is $\propto cos\,(\omega_n t)$, whereas the dispersion component is $\propto sin\,(\omega_n t)$. The dispersive part vanishes at resonance and undergoes a change of sign by going through resonance. Accordingly, this signal is used as an error signal and stabilised at the zero crossing by a feedback loop of PI or PID[7] regulators.

In the actual experiment, the sidebands, created by the EOM, have a modulation frequency of $\omega_m =$21.4MHz. As it turned out, the quality of the error signal can be improved by inserting a polarizing filter directly after the EOM, as the polarization axis is thereby well linearly defined and any circular contributions, introduced by the EOM are damped.

The laser is stabilised to the $F = 1 \rightarrow F' = 3$ crossover on the rubidium D_2-line (see Fig.3.4 and Fig.3.5). Double-pass AOMs are used to get closer to the cooling transition $F = 2 \rightarrow F' = 3$ and, furthermore, provide easy tuneability of the residual red-detuning from resonance.

Rubidium Repump Laser - home-built external-cavity laser in Littrow configuration:

For the repump laser, a master-slave system consisting of two commercially available semiconducting diode lasers has been built.

The master laser is assembled in a Littrow configuration [27], where a grating[8], sitting on a PZT[9], is used to form an external resonator. The grating´s first-order diffraction beam is sent back into the laser diode. Fig. 3.2 shows such a typical laser assembly, which is widely used in our research group. The main purpose of the grating is to force the laser diode not to emit laser light with a linewidth of 50-100 MHz, but with a much narrower linewidth, of the order of the natural linewidth of, for example, rubidium ($2\pi \cdot 6.065(9)$MHz [15]). The position of the grating is optimised in such a way that the lasing threshold current[10] of the diode is minimized by usually approximately 10-20%. This grating feedback is iteratively established by carefully adjusting fine thread screws, which can be seen in picture 3.2.

Temperature stabilisation is performed by a peltier element which is feedback-controlled by a PID card using a NTC[11] sensor signal. Additionally, the whole adjusting setup rests on an

---

[7]Proportional-Integral-Derivative regulator

[8]holographic reflective grating of 1800 lines per mm, gold coated, Zeiss Inc.

[9]piezoelectric transducer

[10]the current, where the lasing process of the diode starts

[11]RS Components negative thermal conductor (NTC) RS 388-0168
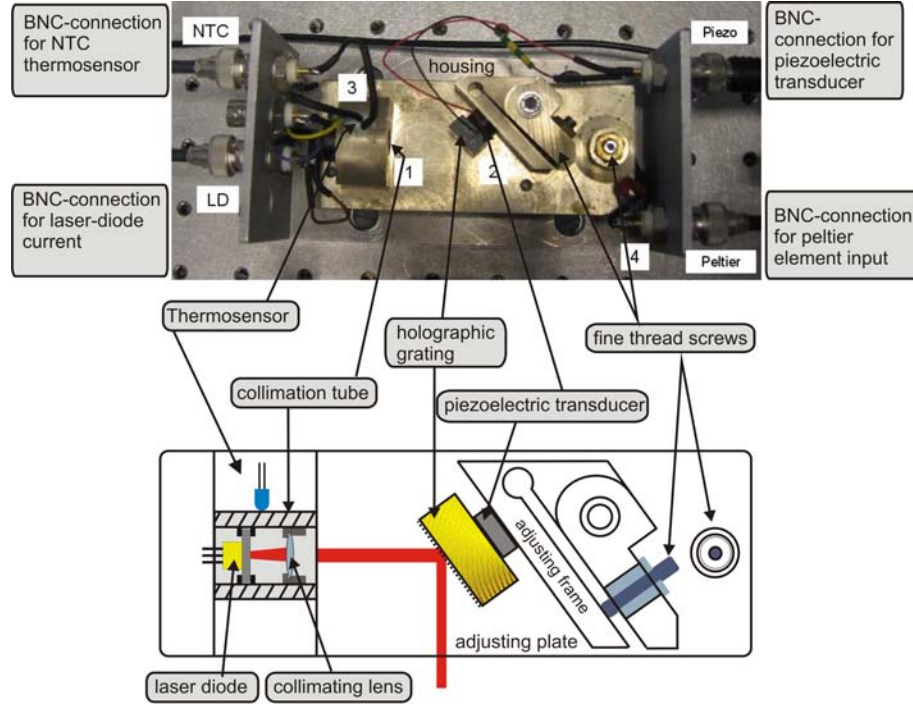
Figure 3.2: Picture and sketch of a typical laser diode housing
1...diode mounting (collimation tube) with collimating lens (aspherical lens, f=4.5mm)
2...grating glued to a piezoelectric transducer mounted on an adjusting frame sitting on an adjusting plate
3...NTC temperature sensor
4...Peltier element input

aluminium block, which can be water cooled. The temperature stabilisation usually works fine at a couple of degrees below room temperature, in our case 18.4°C for the master and 14.5°C for the slave, resulting in a stability of $\Delta T < 1\text{mK}$. This corresponds to a thermal frequency drift of $\Delta\nu < 10\text{MHz}$, as $d\nu/dT = -30\text{GHz/K}$ ($d\lambda/dT = -0.061\text{nm/K}$) [28],

Diode current stabilisation is achieved by using a commercial PID feedback controller, obtaining a stability of $\Delta I < 1\mu A$, which correspond with $d\nu/dI \approx -3\text{GHz/mA}$ [29] to a stability in the order of some MHz.

In order to suppress mechanical deviations of the resonator width, the whole system is composed of as few parts as possible, which are mainly the adjusting frame and the collimation

tube both sitting on the adjusting plate[12]. Furthermore, the system is kept in an aluminium housing, having only a small hole for the laser beam and BNC connectors for the electrical connections. Additionally, the rubidium repump lasers and the potassium lasers are kept in a wooden box, where they are safe from any air turbulence or air flow generated by the air conditioning of the lab.

To secure the laser diode from retro-reflecting beams, which might disrupt normal diode operation and, in fact, kill it, Faraday isolators [30] are placed directly after the output hole of each laser diode housing.

The emitted wavelength of the diode depends on the diode current, the diode temperature and the angle of the external grating. These settings are chosen such that no mode hops occur in the vicinity of the desired wavelength (780.24nm for ^{87}Rb). A detailed discussion on semiconductors and semiconducting laser diodes can be found in [31, 29]. In scanning mode, the wavelength may then be scanned over approximately 1GHz by altering the length of the external resonator using the PZT.

Rubidium Repumper - Lock-In Method

In addition to the passive laser frequency stabilisation methods discussed above, an active frequency lock has to be applied, in order to fulfill the frequency requirements mentioned in section 3.2.1. In frequency-locking mode, a PID controller is supplied with an error signal (generated by a lock-in amplifier, see below), that is set to zero at the desired lock point and shows linear behaviour around the lock point. Using this setup, a linewidth smaller than 1MHz can be obtained and be stabilized over hours.

A lock-in amplifier [32] is used to generate a derivative signal of the spectroscopy signal by modulating the laser diode current with a small amplitude. This derivative signal can serve as an error signal for locking, as spectroscopic peaks are now represented by zero crossings with linear behaviour around the lock point. A lock-in amplifier is a phase-sensitive detector, that measures AC amplitudes, even in the presence of large noise amplitudes, and outputs a DC signal that is proportional to the amplitude of the input signal [33]. Unfortunately, lock-in amplifiers are expensive. A less-expensive laser locking method is the so-called polarization-lock, which requires only a few optical components and relatively cheap electrical circuits for

---

[12]made out of German silver (Cu/Ni/Zn)

the amplification of two photodiode signals [34, 35]. The advantage of wider tunability and capture range is accompanied by the disadvantage of a lower frequency stability of the lock point [36].
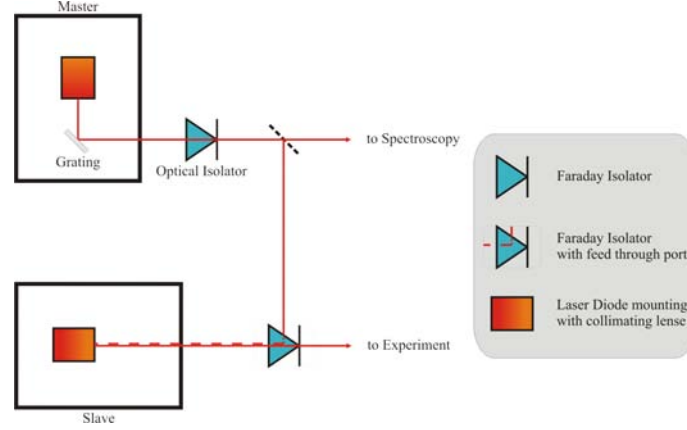
Figure 3.3: Sketch of master-slave layout for the Rubidium Repump Laser.
The master laser, which is stabilized using rubidium spectroscopy and a lock-in amplifier, seeds the slave laser. Diagram based on [23].

Rubidium Repumper - Master-Slave layout

The layout of the master-slave system is illustrated in Fig. 3.3. The master laser, with an output of 50mW, seeds a slave laser. To achieve this, and still secure the diode from any back-reflecting beams, a 40dB Faraday isolator[13] with a side-port[14] is used. The slave laser is thereby injection-locked.

Spectroscopy and Rubidium Level Scheme:

As explained in section 2.1.1, an atom with a two-level system, consisting of an excited state and a ground state can be easily laser-cooled. In the case of the ^{87}Rb D_2 line, nature provides us with a six-level-system hyperfine structure, which can be found in Fig. 3.4. Due to the selection rule $\Delta F = 0, \pm 1$ (of electric dipole transitions) an atom in the excited $F' = 3$ state is only

---

[13]Linos, Inc.

[14]a feed-through port for the laser beam of the master laser
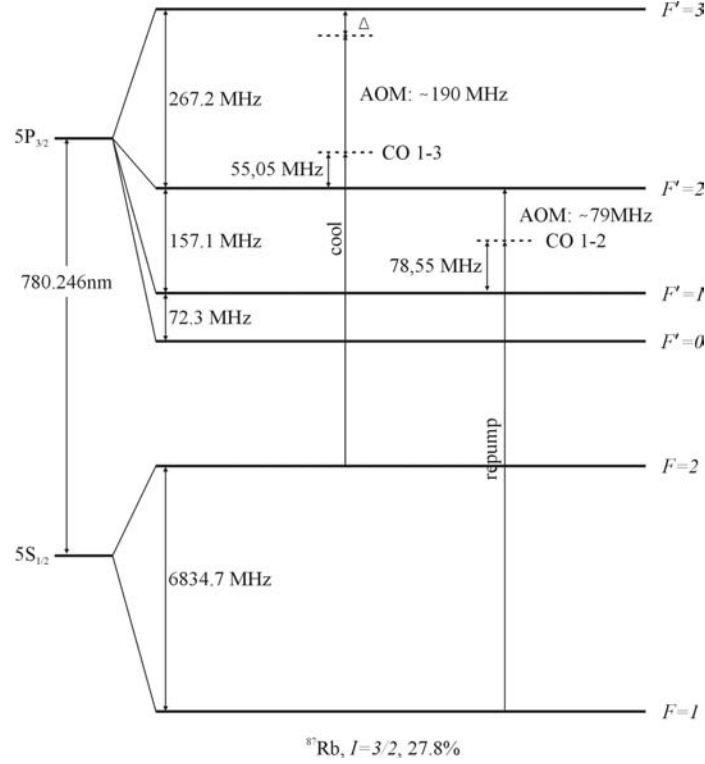
Figure 3.4: Rubidium-87 level scheme of the D_2 line and laser lock points

The cooling laser is locked to the 1-3 crossover (CO) peak of the spectroscopy and shifted with an additional double-pass AOM by an additional 190 MHz, where it is still red-detuned from the $F = 2 \rightarrow F' = 3$ resonance by approximately 22 MHz. The detuning can therefore be easily controlled using the AOM frequency shift.

In the same manner, the repump laser is locked to the 1-2 Crossover peak of the spectroscopy and shifted by a single-pass AOM by an additional 79 MHz, to be approximately on resonance with the repumping $F = 1 \rightarrow F' = 2$ transition.

allowed to fall back into the $F = 2$ ground state. Therefore, by driving the $F = 2 \rightarrow F' = 3$ transition, a closed cycling transition $F = 2 \leftrightarrow F' = 3$ can be generated. Unfortunately, as the levels $F' = 2$ and $F' = 3$ are separated by 267.2MHz and the cooling beam is usually operated such that it is red-detuned, there is still a small probability of obtaining off-resonant excitations into the $F' = 2$ state. From the $F' = 2$ state a fraction of the atoms fall into the $F = 1$ state. These atoms are completely lost from the cooling cycle as the $F = 1$ state is 6.8GHz from the F=2 state. The fraction of atoms in this dark state will increase over time, until the cooling

mechanism extinguishes completely. To avoid this, a second frequency has to be used which pumps the atoms back into the cooling cycle, by driving the $F = 1 \rightarrow F' = 2$ transition. This is the so-called repump laser.

The rubidium vapour cells used for the saturation spectroscopy [13, 10], were manufactured by the glass-blowing workshop in Heidelberg. They are filled with rubidium in natural abundance ($^{85}Rb : 72.17\ (2)\%$ [37], $^{87}Rb : 27.83(2)\%$ [15]) under a pressure of the order of magnitude of 10^{-2}mbar.

Typical ^{87}Rb saturation spectroscopy and error signals are shown in Fig. 3.5. The $F' = 1, 2$ and the $F' = 1/F' = 2$ crossover peaks are not very well pronounced in the absorption signal, but can be easily seen in the error signal. Crossover peaks are usually more pronounced than the actual Lamb dips, and their error signals exhibit greater amplitudes. Therefore, they are preferably used as laser lock points. In our case, the cooling MBR laser is locked to the $F' = 1/F' = 3$ cross over peak and subsequently shifted by a double-pass AOM by an additional 190MHz, hence still being red-detuned by approximately 22MHz to the $F = 2 \rightarrow F' = 3$ resonance.

Consequently, the repump laser is locked to the 1-2 cross over and shifted by a single-pass AOM by appr. 79MHz on the $F = 1 \rightarrow F' = 2$ resonance. A typical spectroscopy trace of the master laser can be found in Fig. 3.6.

3.2.3 Potassium Laser System

Fig. 3.7 illustrates the setup of the potassium laser system. As single high-power laser diodes are not available on the market, two commercial diode laser, of the same type, are used. The DLX110[15] is an external cavity diode laser system utilizing a tapered amplifier diode, which is anti-reflection coated on the back facet. A diffraction grating provides the feedback, as the first diffraction order is fed back into the back facet. This setup results in a higher power than a single laser diode, in our case approximately 450mW.

---

[15]Toptica, Inc., spec sheet: http://www.toptica.com/index.php?categorie=1&itemid=34&linkitemid=1091 (accessed 10.04.08)
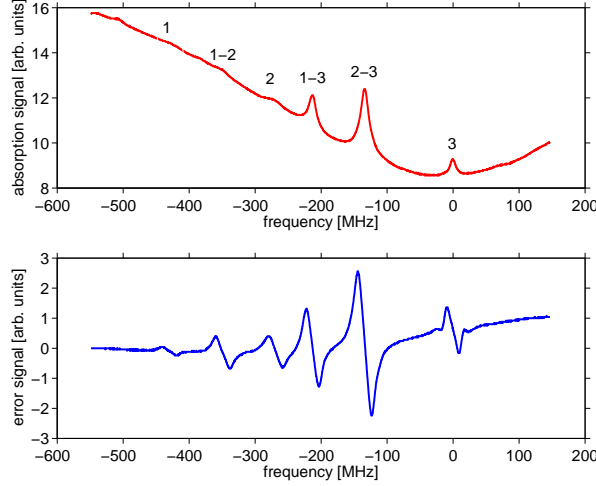
Figure 3.5: Traces for absorption and error signal of the ^{87}Rb cooler transition $F = 2 \rightarrow F'$ taken with the MBR

The peaks in the absorption signal are labeled by the appropriate F' number. Cross over peaks are indicated by the two generating excited-states. The peak corresponding to the cooling transition $F = 2 \rightarrow F' = 3$, has been selected as the frequency reference point.

Potassium Repump Laser - FM Lock

The potassium repump laser is locked by a FM-lock technique (see locking of the rubidium cooling laser in sec. 3.2.2) to the $F = 2 \rightarrow F'$ transition on the D_2-line of ^{39}K. The reasoning behind this decision is mainly that less power is actually needed by the experiment in the repump beam and that the frequency modulation delivers a decent error signal slope for this transition. As can be seen in Fig. 3.7, some light is taken out of the repump beam at the first PBS behind the laser. This light is shifted +312MHz by a double-pass AOM, and then split into two. One part is used for saturation spectroscopy and the other for the frequency-offset (FO) lock of the potassium cooler, which will be described in detail later in this subchapter.

The sidebands for the FM lock are provided by the electronic modulation of the laser current, via a bias-T and at a frequency of 21.4MHz. The error signal is fed to a PI regulator, which acts on the grating and on the current of the laser diode. A typical potassium spectroscopy trace with error signal and lock points can be found in Fig. 3.11.
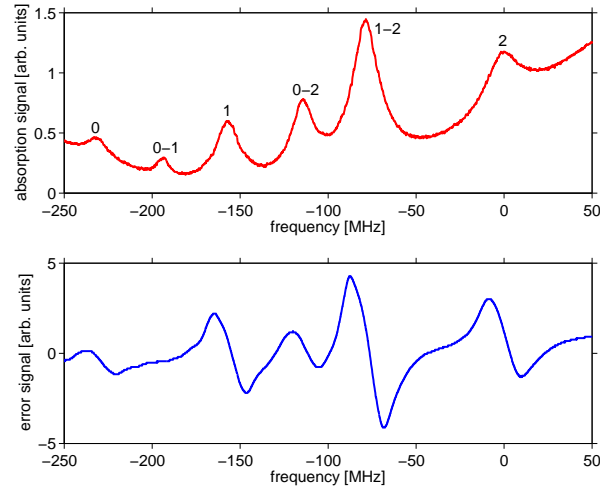
Figure 3.6: Rubidium repumper spectroscopy and error signal staken with the master laser The peaks in the absorption signal are labeled by the appropriate F' number. Crossover peaks are indicated by the two related excited-states. The peak corresponding to the repump transition $F = 1 \rightarrow F' = 2$, has been selected as the frequency reference point.
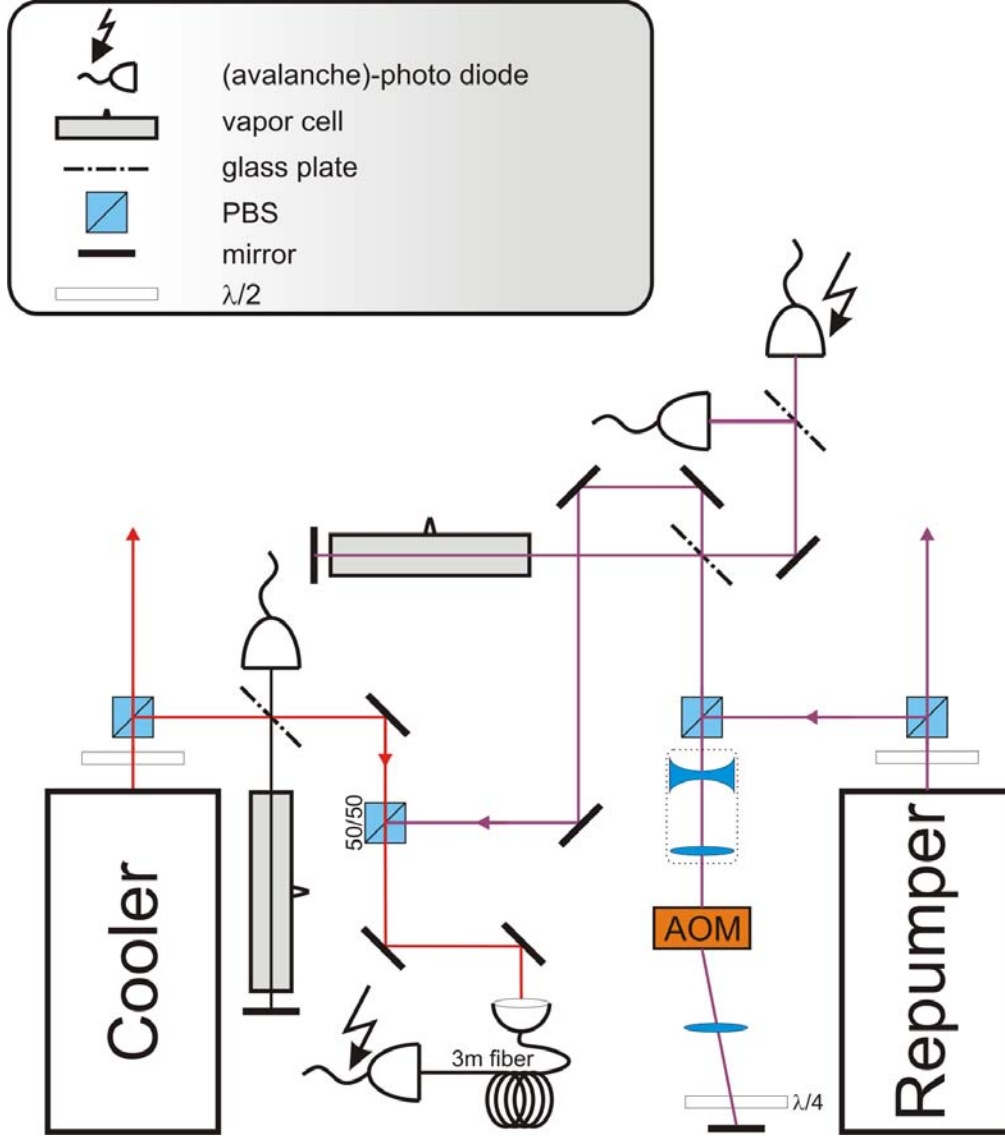
Figure 3.7: Schematics of the potassium laser system

5% of the light of the repumping beam is guided through a double-pass AOM, shifting its frequency by -312MHz, before being split into two. One part is used for saturation spectroscopy and the other part is overlapped with a fraction of the cooling laser beam. This light is then incoupled into a 3m-long fiber forming a beatline for the two beams. The beat signal is detected with an avalanche photodiode. This beat signal is used to fix the frequency difference between the two lasers. The repumper is locked with an FM lock and therefore stabilizes the cooling laser frequency with the FO lock. Diagram based on [23].

Potassium Cooling Laser - FO Lock

The potassium cooling laser is locked using a frequency-offset (FO) lock [38] because a FO lock needs only low intensities and exhibits easy and wide tuning possibilities. The loss of light for a double-pass AOM, needed for a sufficient frequency shift away from lockable ^{39}K transitions, is thereby avoided.

The FO lock uses the beating signal between two lasers to fix the frequency difference between the two sources. In our case, the repump laser is used as a stable reference frequency source that stabilizes the cooler. Depending on the application, the beating frequency $\Delta\nu$ might be between 10MHz and several GHz. In the case of high beat frequencies, it is convenient to transfer them down into a frequency domain below 100MHz, where comparably cheap electronic components may be used. In the current setup, this transfer is performed by mixing the frequency $\Delta\nu$ with the frequency of a voltage controlled oscillator ν_{VCO}, which gives $\Delta\nu\pm\nu_{VCO}$. Subsequently, a low-pass filter selects the $\Delta\nu - \nu_{VCO}$ component. The signal is then split into two equal parts and one part is delayed with an approximately 4m long coaxial cable, resulting in a delay time τ of 20ns[16] and a phase difference of

$$\Delta\phi = 2\pi\left(\Delta\nu - \nu_{VCO}\right)\tau. \tag{3.7}$$

A phase detector compares the two components and outputs $U \propto cos\left(\Delta\phi\right)$. This output is used as the error signal. The zero crossings $cos\left(\Delta\phi\right) = 0$ can be used as locking points. This gives

$$\Delta\phi = \left(n + \frac{1}{2}\right)\pi \tag{3.8}$$

and by inserting eq.3.7

$$\Delta\nu = \frac{2n+1}{4\tau} + \nu_{VCO}. \tag{3.9}$$

The spacing of the zero crossings is

$$\frac{1}{2\tau}, \tag{3.10}$$

---

[16]the signal propagation velocity in the coaxial cable can be approximated by 2/3 of the velocity of light c

but as the PI lock electronic may only lock on either a positive or a negative slope of the error signal, the spacing of the locking points is $1/\tau$. The position of the locking points can be altered by changing the frequency of the voltage controlled oscillator ν_{VCO}. Therefore frequency sweeps for atom number determination can be performed easily.

The optical layout of the FO lock can be found in Fig.3.7. A glass plate subtracts 5% of the light to be used for the saturation spectroscopy using a heated vapour cell. The remaining fraction of the light is overlapped at a 50/50 beam-splitter cube with the repumper beam and together coupled into a 3m-long polarization-maintaining single-mode fiber. The fiber becomes a beatline for the two beams, which have equal polarizations and are well spatially overlapped. Even with beam intensities of approximately 300μW, a large beating signal, at a frequency of approximately 1GHz is generated. This signal is detected using a fiber-coupled avalanche photodiode.

Fig. 3.8 illustrates the electrical layout of the FO lock. The detector output signal is amplified and mixed with a local oscillator. The FO-card generates the error signal, which is again filtered by a low-pass and used as an input for a PID card.

Further details on the FO lock technique and the design of the home-built local oscillator can be found in [23] and references therein.

Potassium level scheme and spectroscopy

The potassium vapour cells, used for saturation spectroscopy [13, 10], were manufactured by the glass-blowing workshop in Heidelberg. They are filled with potassium in natural abundance ($^{39}K : 93.258(4)\%$ [37], $^{40}K : 0.012\%$ [15], $^{41}K : 6.730(4)\%$ [37]), at a pressure of the order of magnitude of 10^{-2}mbar. As the vapour pressure is different for potassium and rubidium [39, 15], potassium vapour cells need to be heated in order to increase the peak-to-peak amplitude of the error signal of the FM lock. In Fig. 3.9a the peak-to-peak amplitude of the error signal is plotted against the temperature of the vapour cell. At 42°C, the error signal amplitude is increased by a factor of approximately 4, compared to room temperature values, thus resulting in a sufficiently large error signal and stable lock, with negligible air turbulence around the cell. Further increasing the cell temperature leads to a decrease in the error signal´s amplitude, as the cell becomes optically opaque. A typical vapour cell, packed in its heating compartment with an insulation layer of aluminium foil, is shown in Fig. 3.9b. To avoid any potassium
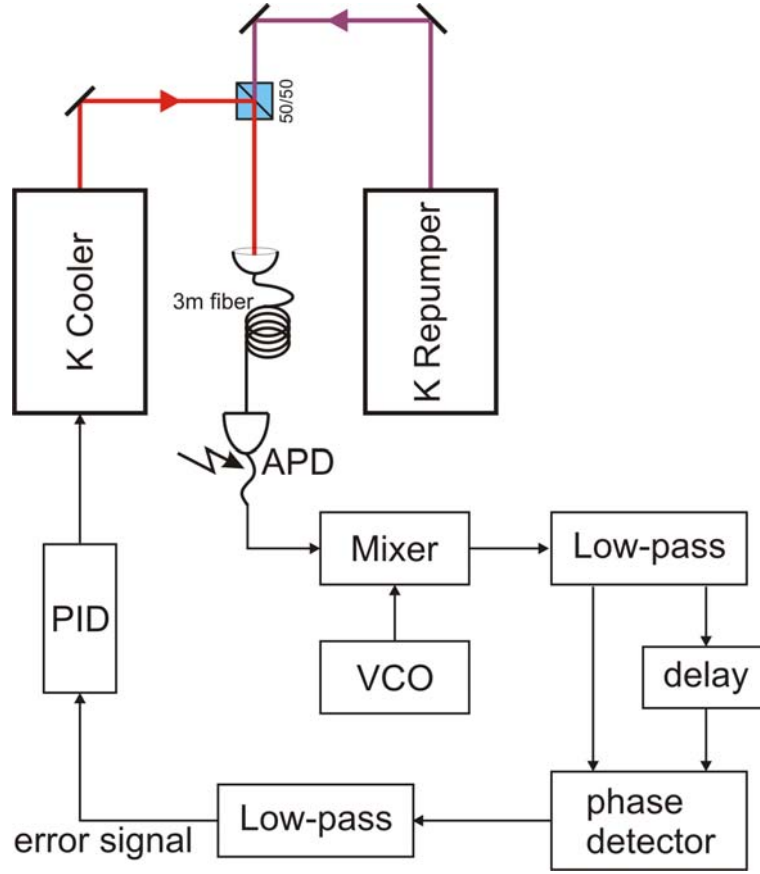
Figure 3.8: Layout of the frequency offset of the potassium cooling laser
The detector output signal is amplified and mixed with a local oscillator (VCO). The phase detector compares the delayed signal with the direct signal and generates the error signal, which is again filtered by a low-pass. A PID regulator is used to lock the laser with the error signal.

coating of the windows, a cold spot has to be maintained. This cold spot is currently at the point where the cell was filled and a glass nipple was left remaining.

Fig. 3.10 shows the hyperfine levels of the D_2 line of ^{39}K and ^{40}K . One astonishing feature of ^{40}K is that its hyperfine structure is, in terms of level-energy, inverted. Low F numbers correspond to high energy. The reason for this inversion and the other differences between ^{40}K and ^{87}Rb are discussed in detail in chapter 4.3.1.
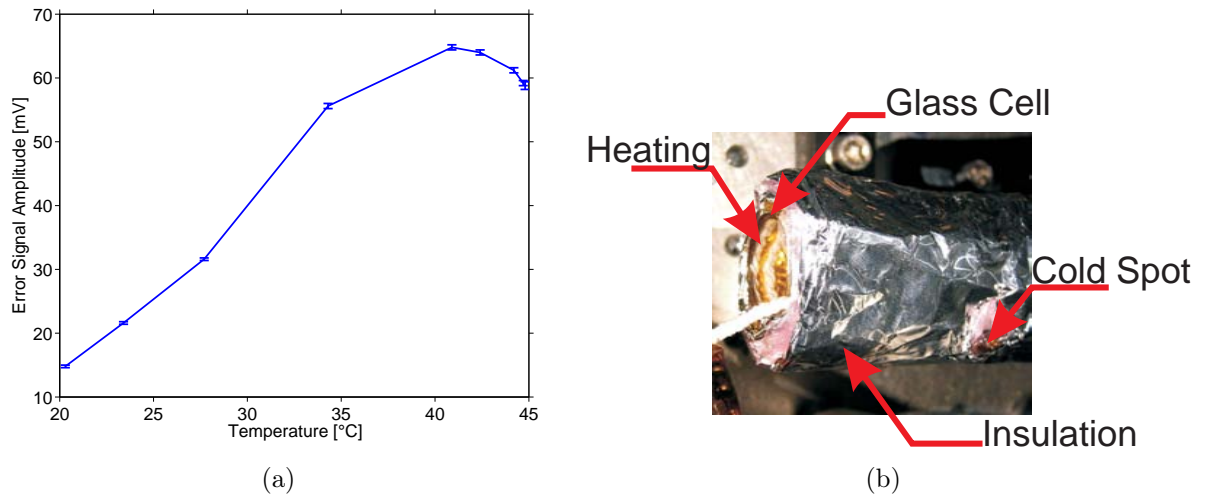
Figure 3.9: Dependence of the error signals amplitude on the potassium vapour cell temperature and a photograph of a potassium vapour cell

(a) A maximum of the amplitude of the error signal is found at 42 °C. To guide the eye, lines connecting each data point are plotted.

(b) A picture of the potassium vapour cell, filled with potassium in natural abundance (^{39}K : 93.258(4)% [37], ^{40}K : 0.012% [15], ^{41}K : 6.730(4) [37]) is shown. The heating wires, the insulation and the cold spot can be clearly seen. Diagram provided in collaboration with and picture based on [23].
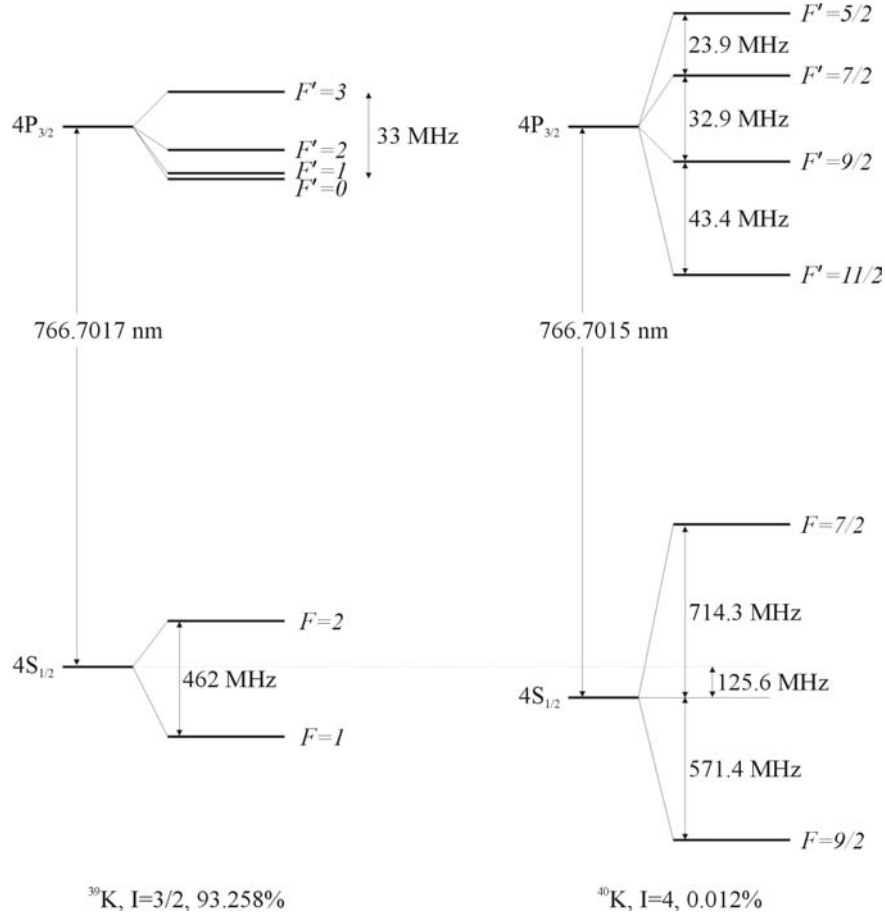
Figure 3.10: ^{39}K and ^{40}K level scheme

The hyperfine level scheme of the fermionic potassium isotope ^{40}K is inverted compared to the bosonic potassium isotope ^{39}K. The level spacing of ^{39}K is very tight and difficult to resolve by saturation spectroscopy. The nuclear spins and the natural abundances of the two isotopes are given [37]. Due to the small abundance of ^{40}K, enriched dispensers (5.5%) have to be used in the collection chamber, in order to sublimate enough trappable atoms.

A typical potassium spectroscopy trace with error signal and lock points is illustrated in Fig. 3.11.
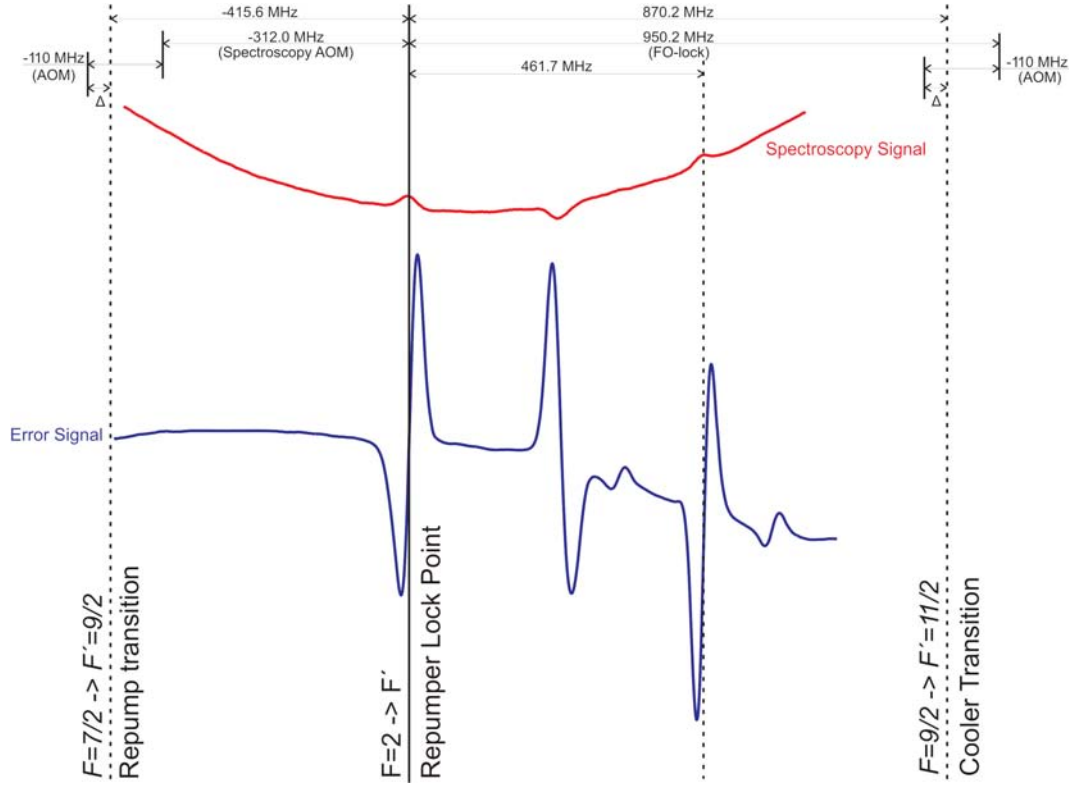
Figure 3.11: Potassium spectroscopy and locking scheme

The repumper is locked to the D_2-line $F = 2 \rightarrow F'$ transition of ^{39}K, where the frequency scale is set to zero. The ^{40}K cooler $F = 9/2 \rightarrow F' = 11/2$ and repumper $F = 7/2 \rightarrow F' = 9/2$ transitions are indicated by vertical dashed lines. Typical traces of the spectroscopy and of the error signal are shown. The frequency shifts performed by the different AOMs and the FO-lock are depicted. Diagram based on [23].

3.2.4 Optical Tables

Two air-cushioned optical tables[17] have been installed in our lab. The so-called laser table houses the five lasers needed for the experiment, and a decent quantity of optical components. The two potassium lasers and the rubidium repumper master-slave system are housed, together with their spectroscopy vapour cells, in a wooden box, damping outside acoustic noise and keeping them safe from any air turbulence. The rubidium cooler Verdi-MBR ring laser system[18]

---

[17]Thorlabs, GmbH
[18]Coherent, Inc.

is resting on the other end of the table. In between the wooden laser box and the Verdi-MBR system a huge optics park (see Fig. 3.12) has been established. The setup of the optical bench is shown in Fig. 3.13. The main purpose of these optical components is to split the initial beams, pass them through AOMs[19], overlap them with their counterparts[20] and, finally, feed them into polarization-maintaining (PM) optical fibers that carry the beams to their appropriate application on the experimental table. The five PM fibers are dedicated for the collection MOT (see chapter 4), the mirror MOT, the push beam, imaging, and optical pumping.

The vacuum apparatus (see section 3.3) with the bias and compensation coils (see subsection 3.4), the MOT (compare section 3.5) and imaging optics, and the cameras are situated on the experimental table. This is where everything comes together and eventually a degenerate Bose-Fermi mixture will be formed.
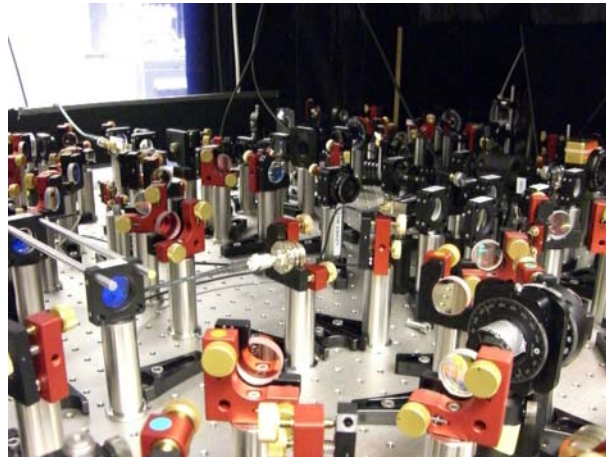
Figure 3.12: Optics park

---

[19]despite using AOMs for frequency shifting, they are also used, together with shutters, to switch beams on and off

[20]for example, overlap potassium light (cooling and repumping light) with rubidium (cooling and repumping) light, which is then used to form a dual-species MOT
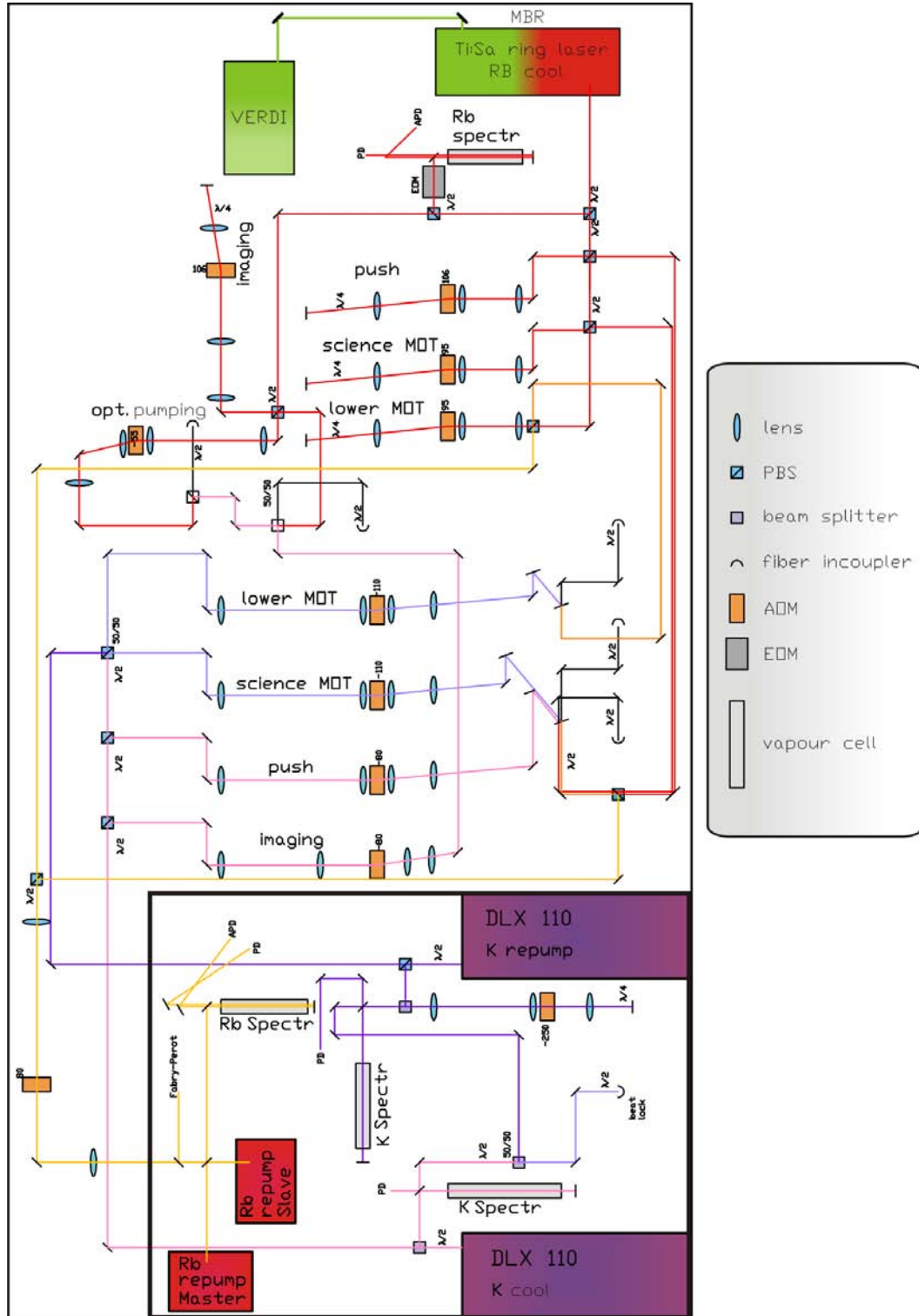
Figure 3.13: Laser Table Setup

3.3 Vacuum System

3.3.1 Overview

This section describes the two-chamber vacuum system, consisting of a collection chamber, with the atomic sources, and a science chamber, where the atomchip is situated and a degenerate Bose-Fermi mixture will be produced. The unique new design of the Science Chamber exhibits optimised optical access to the trapping region. The advantages of this two-chamber setup will be discussed in detail. Finally, the almost never-ending and time-consuming problems that occurred with the vacuum windows of the science chamber are reported.

3.3.2 The Two-Chamber Setup

The vacuum system consists of a two-chamber apparatus, where a collection MOT feeds a science MOT via a push laser beam through a differential pumping stage.

The Collection Chamber

The collection chamber acts as an atom source for the actual experiment, carried out in the science chamber. It houses commercial rubidium[21] and home-built, enriched (^{40}K: 5,5%) potassium dispensers. Ohmic heating of the dispensers leads to a degassing of atoms, providing the necessary background pressure for the subsequent cooling and trapping in the collection MOT.

The manufacturing of the home-built potassium dispensers (see Fig. 3.14) is presented in detail in [23], only the working principal shall be briefly discussed here. The mixture of enriched, pure KCl[22] and pure Ca, both in powder form, undergoes a reduction reaction triggered by heating

$$2KCl + Ca \rightarrow 2K + CaCl_2, \tag{3.11}$$

releasing potassium atoms into the vacuum, but capturing Cl-atoms in $CaCl_2$.

The shape of the collection chamber might be described as hedgehog like, as can be seen

---

[21]from SEAS Getters, Inc.
[22]obtained from Trace Science International

Figure 3.14: Picture of the home-built potassium dispensers

The enriched *KCl - Ca* powder mixture is located in a NiCr boat. Two dispenser boats are connected in parallel and mounted an a Marcor ceramic plate, which ensures that there is no electrical connection between the collection chamber and the dispensers. By applying a current of 7A, the dispensers are heated and a reduction reaction (see text) emitting potassium atoms is triggered.

in Fig. 3.15. It consists of six DN40CF viewports[23], used for the six-beam retro-reflection MOT, and eight DN16CF ports. One of the DN40CF ports is connected via a T-piece to an ion pump[24]. Two of the DN16CF ports house the two pairs of dispensers, where the dispenser currents are provided by electrical feedthroughs. For a single dispenser pair, the two dispensers are mounted in parallel on a ceramic Marcor[25] spacer to prevent electrical contact with the chamber. Two other DN16CF flanges are connected with two all-metal valves, one being the connection to the science chamber through a differential pumping tube, and the other being the connection to the outside world, where a turbomolecular pump can be attached. The remaining DN16CF flanges are sealed with standard DN16CF viewports, where photodiodes (compare 4.2.1) and CCD cameras can be placed.

The quadrupole field for the collection MOT is generated by two coils[26], which are directly wrapped around two opposing DN40CF tubes of the vacuum chamber. Furthermore, three pairs of compensation - shift coils are attached to each flange, creating a homogeneous magnetic field. These coils provide the possibility of shifting the the zero point of the quadrupole field, being the trapping center, in all directions. This procedure is used for alignment purposes of the

---

[23]DN40CF viewports are sealed by standard uncoated windows

[24]Varian 20l/s Star-Cell ion pump

[25]UHV proofed, ceramic spacer, supplied by

[26]Two coils of insulated copper wire of 1.5mm diameter with 90 turns. The calculated gradient in the trap center is 4G/cm/A
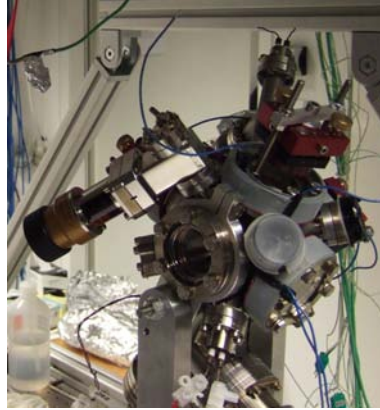
Figure 3.15: Picture of the collection chamber

On the left hand side, an all-metal valve can be seen, where the differential pumping stage and the science chamber will be connected to. In the front a DN40CF viewport, used for one of the MOT beams, can clearly be seen. Below this window, one can see the connections of the rubidium dispensers. From the Rb dispensers point of view, directly on the opposite side, are the potassium dispensers located. The window at the top has got a compensation coil wrapped around it. Additionally, one of the retro-reflecting mirrors is mounted there on two threaded rods. At the bottom, an ion pump is connected at the T-piece, which is almost hidden by the broad aluminium mounts of the chamber itself.

trapping center of the MOT with respect to the push beam axis. The optimal alignment is found by optimising the loading rate of the science MOT.

The Science Chamber

The design of the science chamber exhibits optimised optical access to the trapping region with two large windows, each with a diameter of 100mm, and three smaller windows, each with a diameter of 43mm. The distance from the chip center to the inner surface of the large window is 41.5mm and the distance to the inner side of the small window is 80mm. The chamber was constructed out of a single block of steel. The AR-coated quartz windows are sealed using copper Helicoflex Delta seals supplied by Garlock. The atom chip is situated 15mm above the center of the two larger windows on the horizontal axis. For further information on the design and finite-element simulations of the deformations of the chamber, please refer to [23].

The installation of the two chambers is illustrated in Fig. 3.17. The top of the science

chamber is connected via two opposing DN200CF ports to the so-called pumping part, with an ion pump[27] and a TSP[28]. One of the six DN40CF ports on this chamber is used for a UHV[29] Bayard-Alpert-type ion gauge, and another one for an all-metal valve, sealing the chamber. The remaining ports are sealed with DN40CF blank flanges and one DN40CF viewport.

(a)   (b)
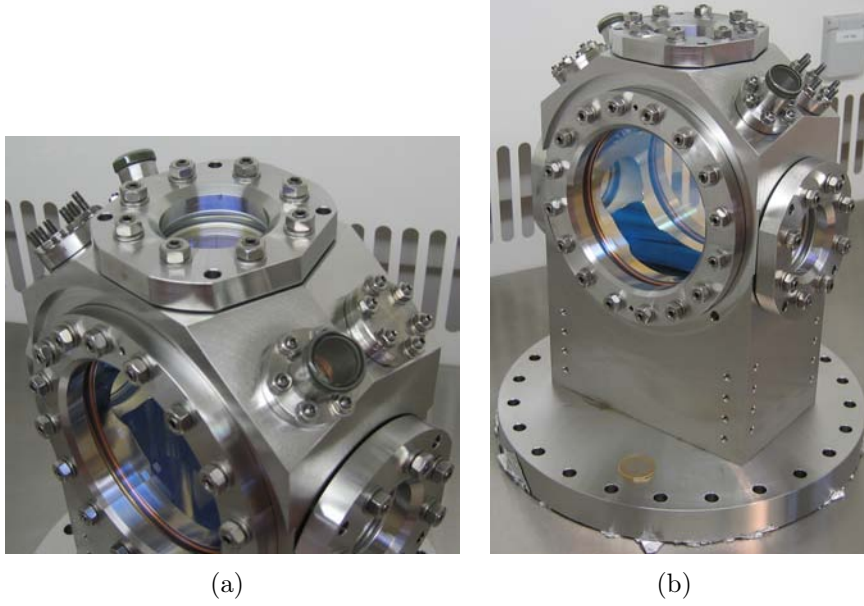
Figure 3.16: Photographs of the science chamber

Science chamber after assembly in the clean-room environment.
(a) Top view of the science chamber, which was manufactured out of one block of stainless steel. Custom-made Helicoflex delta seals are used for the windows.
(b) In the bottom part, the DN200CF flange that was welded on the science chamber block can be seen.

Tha Advantages of the two-MOT Setup

The collection MOT loads from the background pressure generated by the dispensers, whereas no dispensers[30] need to be present in the science chamber as the science MOT is loaded directly

---

[27]Varian Star Cell 150l/s

[28]Titanium Sublimation Pump

[29]ultra high vacuum

[30]dispenser sources always spoil vacuum at UHV conditions and would result in the need of high pumping speeds and a larger cross section of the connection to the pumps, thereby the whole science chamber would
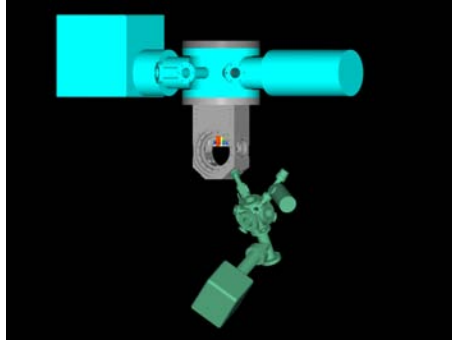
Figure 3.17: CAD drawing of the complete vacuum assembly
From top to bottom: The pumping part with an ion pump (big box) and a TSP (inside the tube on the upper right-hand side).
The science chamber is connected via a differential pumping tube to the collection chamber, which is connected to a small ion pump.

via the push beam. In the collection chamber, the typical pressures are $10^{-8} - 10^{-9}$mbar and in the science chamber, 10^{-11}mbar . Therefore, the advantages of this two-chamber-design are

- low background pressure in the science chamber

- longer lifetime in the magnetic trap

- independent loading control of the two species into the science MOT via the push beam

3.3.3 The Atom Chip

The atom chip is mounted on a ceramic[31] mount, which was manufactured in Heidelberg. The mounting consists of large-scale copper structures, used for macroscopic traps and an atom chip, used for microscopic traps. Furthermore, the mounting provides all electrical connections for the copper structures and atom chip trapping and manipulation wires. Fig. 3.18 shows some pictures taken of the chip mounting. The copper structures can clearly be seen. The copper U structure forms, together with the externally provided homogeneous magnetic bias

become bigger.

[31]Shapal, a machinable ceramic, which combines a high thermal conductivity with a high mechanical strength. Furthermore it is UHV compatible.

fields, a quadrupole magnetic field, used for the mirror MOT (see subsection 3.5.2). Z-shaped wires are used to form magnetic traps of the Ioffe-Pritchard type. Macroscopic magnetic traps, microtraps and microtrap implementations using atom chips are presented in [23, 40, 41, 42]. A nice overview of magnetic microtraps for ultracold atoms is given in [43].
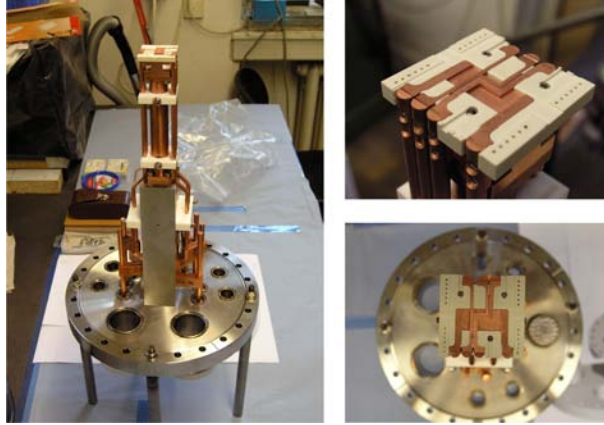
Figure 3.18: Atom chip mounting

The atom chip itself was fabricated by standard microfabrication technology and has a gold layer of a height of approximately 3μm at trapping wire widths of 10-200μm. Fig. 3.19 shows the design of the atom chip. Six trapping wires can offer radial frequencies in the tens-of-kHz range. Furthermore, it is possible to create axial trapping frequencies of less than 1Hz, thereby obtaining high aspect ratios in the order of 10^4. A detailed discussion of the design and fabrication of the atom chip used in our experiment may be found in [44].

3.3.4 Implementation of Optics and Infrastructure around the Completed Vacuum Chamber

Fig. 3.20 shows an AutoCad[32] plot of the final design of the experiment. The whole vacuum apparatus rests on a frame of high-tensile aluminium profiles[33]. Additionally, optics boards[34]

---

[32]Autodesk, Inc.

[33]all profiles, connections and construction components are supplied by item Industrietechnik GmbH, www.item.info

[34]Thorlabs, Inc.
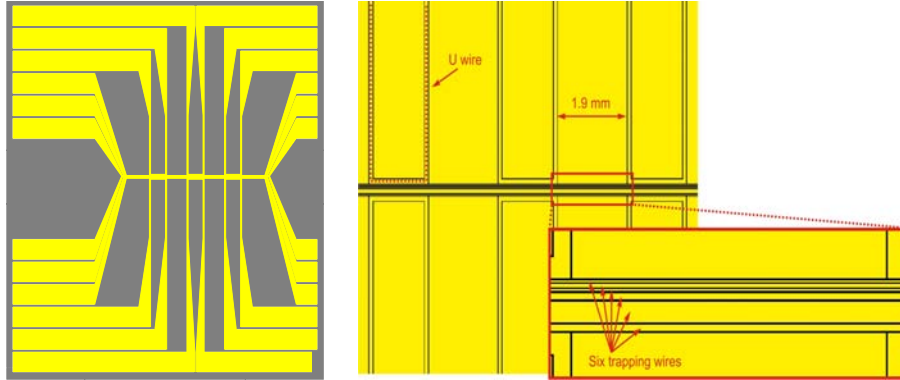
Figure 3.19: Design of the atom chip used in this experiment

Six trapping wires offer radial frequencies in the tens-of-kHz range together with axial frequencies smaller than 1Hz, providing high trapping frequency aspect ratios of 10^4.

have been machined to fit between the item bars and the coils. The MOT optics and the imaging systems are mounted on these boards.

3.3.5 The Window Problem

In order to evacuate a vacuum chamber and reach a decent UHV pressure of $< 10^{-11}$mbar (see subsection 3.3.2), the chamber has to be baked-out during evacuation. Increasing the temperature increases the rate of the outgassing processes, which depend on the rate of desorption, diffusion and permeation processes [45, 46].

Choosing the upper limit of the bake-out temperature depends on the vacuum chamber design. Standard vacuum apparatuses are heated up to 200-250°C, but, as the science chamber consists of large, sensitive windows, the initially intended bake-out temperature was about 150°C. This decision leads to an increase for the necessary bake-out time [45]. Therefore, each baking cycle takes approximately one weak to slowly heat the chamber, three weeks at constant temperature and again one weak to cool down to room temperature. Nevertheless, even during this slowly and carefully heating one of the two large windows repeatedly broke three times above 100°C at the same spot, where the seal was located. As the windows are non-standard, they have a lead-time of at least three months, resulting in a substantial loss of time and Gantt charts being thrown upside down.
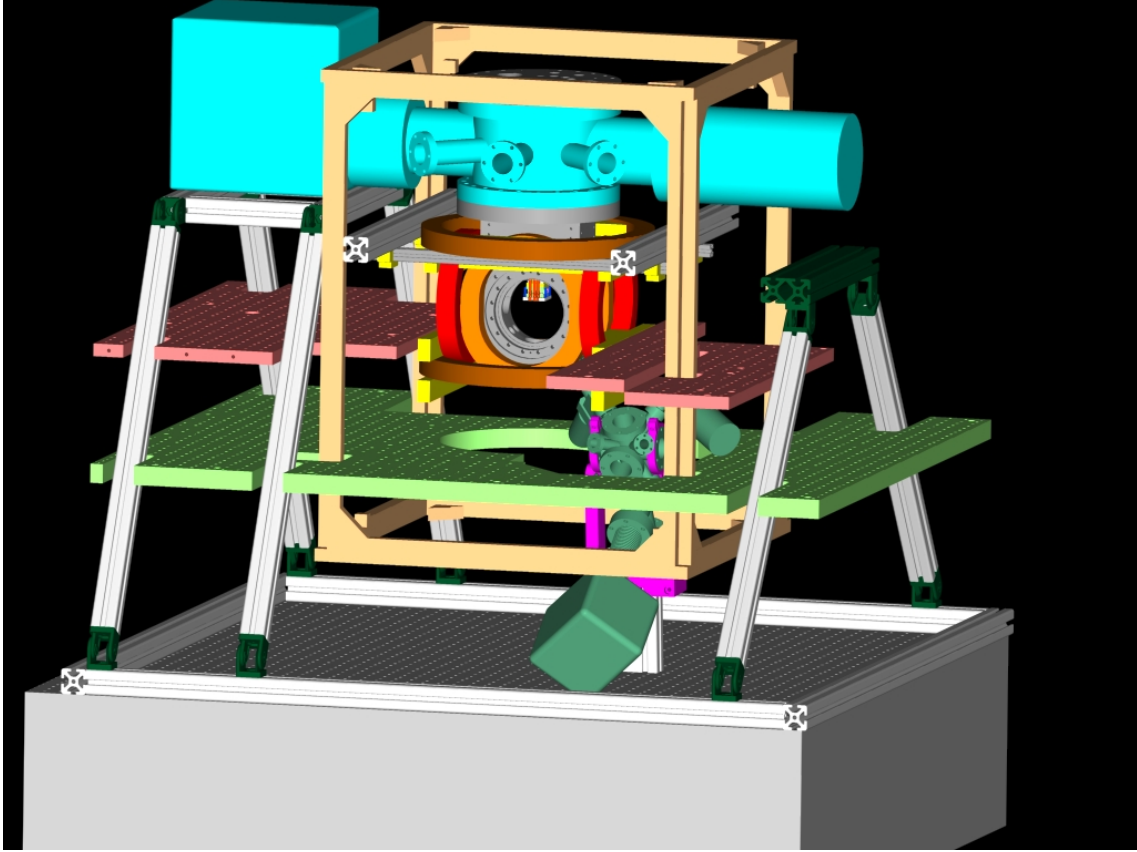
Figure 3.20: Complete experimental assembly

In order to find the source of the problem, contacts to experienced vacuum engineers and experts have been established. Two of them shall be mentioned here, as they immediately found time to provide us with their advice and experience. Ao.Univ.Prof. Dr.phil. Herbert Störi, being Vice-president of the Austrian Vacuum Society and head of the institute Allgemeine Physik at the Vienna University of Technology and Univ.Doz. Univ.Prof. Dr.phil. Rudolf Dobrozemsky, also known as the "vacuum god" among students. The third attempt was carried out by placing Teflon foil between glass and seal, thus being sure that no dust particle, causing a very local heat and pressure spot on the glass, is causing the problem[35]. Finally, two possible sources had been left:

---

[35]Teflon foil can spread local pressure spots

- the welded connection between the science chamber and the DN200CF flange. As welding causes a very local heating of the steel, tension can be caused in the material that spreads unevenly due to the rectangular, asymmetric shape of the welding.

- the not performed bake-out to >1000°C before the last, final step of the manufacturing procedure, as heavy machining can also generate tensions in the steel matrix.

These tensions can cause deformations during bake-out, thus deforming the contact surface of the Helicoflex Delta seal and putting too much stress on the quartz window. The Helicoflex seal can only compensate the normal difference in temperature expansion between steel and glass, but it cannot compensate deformations in the evenness of the steel surface. The exact reason of the problem remains unknown, but two solutions have been found:

- attaching a metal tube, which could shield any tension and deformations from the windows (see Fig. B.1), with standard viewports

- using instead a 50% thicker (15mm) BK7 glass substrate window without AR-coating

Currently, the second temporary, makeshift solution seems to have become the final one. The adaptor tube was delivered at the end of February 2008 and might still be of use in the future.

3.4 Bias Field Coils

The next part focuses on the external magnetic bias field coils, used together with the broad copper U wires to generate a magnetic quadrupole field for the science MOT. They are also used for the Z traps and also for the chip traps.

3.4.1 Purpose

Three pairs of bias field coils are used to generate homogeneous magnetic fields, needed for the operation of the mirror MOT and the Ioffe-field magnetic traps. Ambient magnetic fields are compensated using large, rectangular compensation coils.

3.4.2   Design, Construction and Testing

The coils, which have to fit around the science chamber, are built as close to Helmholtz configuration as possible. Two pairs of oval coils fit exactly around the horizontal windows and one pair of larger, circular coils is used for the vertical Z-direction as can be seen in Fig. 3.21b. The coils are mounted tightly, conserving the optimised optical access to the trapping region. For the mounting structure, fiber-glass-reinforced epoxy material[36] components, being non-conducting, are used together with A4-grade stainless-steel threaded rods[37].

(a)   (b)
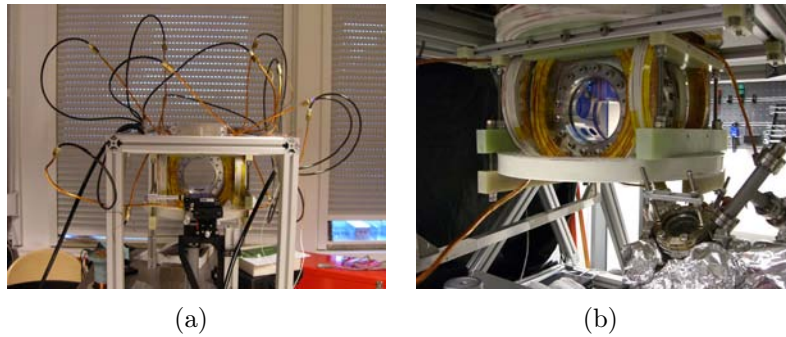
Figure 3.21: Bias coils test setup and final mount around the science chamber
(a) test setup; coils are connected to black water pipes, the current connections are missing on this picture. The three orthogonal translation stages, where the Hall probe was mounted, can be seen at the front. The whole mount is supported by a frame of item bars.
(b) final mount around the science chamber; the green epoxy parts can clearly be seen; parts of the collection chamber can be seen at the bottom.

The coils were manufactured in Vienna by the ATI TU Wien in-house workshop. A hollow copper wire[38], with a quadratic cross section and insulated with Kapton foil on the outside, was used for manufacturing.

Through the hollow copper wires, cooling liquid flows to prevent the coils from ohmic heating and reduce possible mechanical deformations. Additionally, keeping the coils at a constant temperature counteracts temperature drifts in the resistance. To obtain more stability in the strength of the magnetic field, a current feedback control unit, discussed in subsection 3.4.3, was

---

[36]fiber-glass-reinforced epoxy EPG-GC-201, supplied and machined by Hippe, www.hippe.de

[37]supplied by Wasi-rostfrei Schraubenhandelsgesellschaft m.b.H., http://www.wasi.at

[38]Wiresize: 4.4-4.45 mm; wiresize with Kapton insulation layer: 4.6 mm; hole diameter: 2mm; supplied by S&W Wire Company http://www.swwireco.com/

designed. A long-term measurment showed that all six coils can be operated simultaneously at a current of 45A and at constant coil temperature. The inlet cooling liquid temperature was T=12°C at 2bar pressure and the outlet cooling liquid temperature was T=23°C at an ambient room temperature of approximately 24°C.

To save time during vacuum bake-out, the whole coil assembly, the mounting parts and coils, can be safely heated up to 150°, making it therefore unnecessary to remove the structure, if further baking is required.

For testing purposes, the coils and mounts were completely assembled on an extra table, see figure 3.21a. The magnetic field strength in a cube of 864mm^3 in the trapping region was measured with a Hall probe[39], positioned using micrometer translation stages[40]. The results show that the deviations in the magnetic field are below or of the order of 1%. In this cube, the magnetic field strength can be regarded as constant. The contributions generated from one coil pair into the symmetry-axis of another one are below 3%.

Additionally the magnetic fields have been calculated numerically, where the superposition of the 36 turns, taking into account their changing relative position, was calculated. Due to the oval shape of four of the bias coils, a single turn was represented by 1002 small segments. The measured and calculated values are in good agreement (less than 3% deviation) and can be found in table 3.2.

Spatial Direction	Shape	Radius [cm]	Windings #	$B_{measured}$ [G/A]	$B_{calculated}$ [G/A]	Resistance mΩ	Inductance mH
X	oval	7.25	36	2.72 ± 0.01	2.77	100 ± 2	0.28
Y	oval	7.25	36	1.27 ± 0.01	1.24	99 ± 2	0.28
Z	round	15	36	1.71 ± 0.02	1.73	133 ± 2	0.7

Table 3.2: Parameters of the bias field coils

Resitance values are given for each coil pair and the cable connections to the power supplies. Radius gives the inner radius of the coils. Each coil has a cross section of approximately 28*28mm^2.

---

[39]Model 6010 gaussmeter from Sypris Solutions, Inc.
[40]Newport, Inc.

3.4.3 Current Feedback Control for higher Current Stability

To improve the stability of the magnetic traps, a current feedback module was designed [23]. An ultrastable high-current resistor is used for current sensing. The bandwidth of the power supply - coil system, given by the -3dB point in the frequency response, could be improved from approximately 200Hz to approximately 670 Hz, see Fig. 3.22. The feedback system can therefore process fluctuation signals of a bandwidth of 670Hz. The circuit diagrams of the feedback loop can be found in [23].
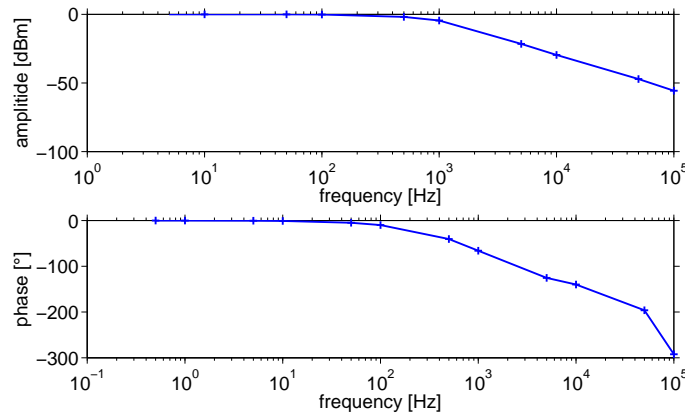
Figure 3.22: Frequency and phase response of the feedback and coil circuit
Data taken with a lock-in detector in collaboration with [23]. The bandwidth of the power supply - coil system, given by the -3dB point in the frequency response, was improved from approximately 200Hz to approximately 670 Hz.

3.4.4 Charge Pump

A charge pump is used to decrease the switch-on time of the bias coils. In principle, a capacitor is charged to a high-voltage and rapidly discharged into the coil. To avoid the formation of a LC-oscillating circuit, the capacitor has to be disconnected by a thyristor after the first quarter cycle of such oscillations. Fig. 3.23 shows the switch-on behaviour of the X- and Z-bias coils. The circuit diagrams of the charge pump can be found in [23].
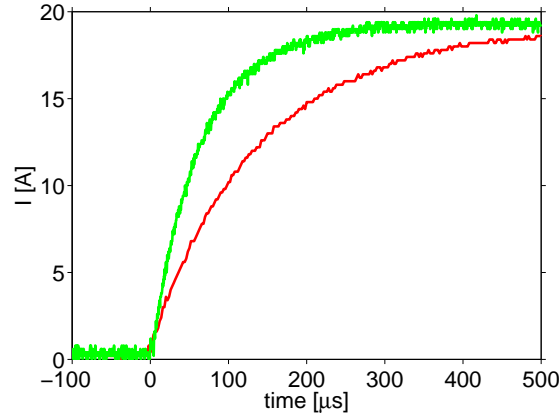
Figure 3.23: Switch-on behaviour of X- (green) and Z- (red) bias coil pairs
For the X-coils, the loading time constant is approximately $65 \pm 1\mu s$ and, for the Z-coils, a higher value of $122 \pm 2\mu s$ is found, due to the higher inductance of the Z-coils (see table 3.2). In collaboration with [23].

3.5 MOT optics

During this diploma work, the science MOT and collection MOT optics assembly have been built up from scratch. The layout of the necessary optic components is illustrated in this section.

The MOT beams for K and Rb are superimposed on the laser table and brought to the experimental table via PM fibers, as described in subsection 3.2.4 and illustrated in Fig. 3.13.

3.5.1 Collection MOT Optics

Fig. 3.24 shows the layout of the two-species collection MOT optics setup, which is a 3D MOT, consisting of six orthogonal beams. To reduce the number of optical components and the space taken by them, the trapping light is retro-reflected for each direction. Each retro-reflecting mirror is mounted with a bar on two threaded rods that replace two M6 bolts of the DN40CF flange, (see Fig. 3.15).
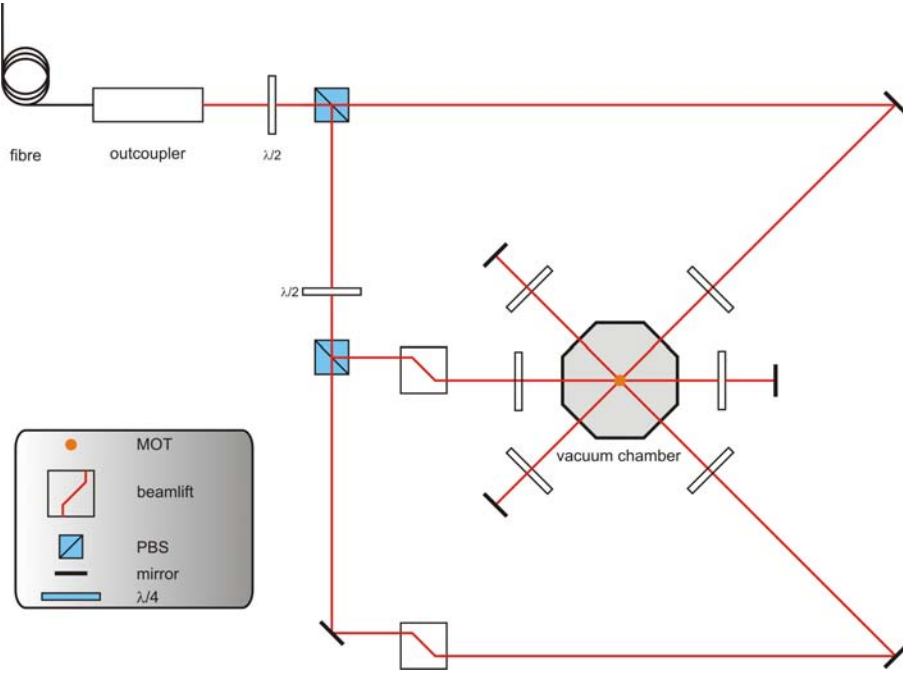
Figure 3.24: Collection MOT optics layout

The Collection MOT is installed in a 3D six-beam retro-reflection setup. The trapping light is retro-reflected for the three directions, in order to reduce the number of optical components and the space taken by them.

3.5.2 Science MOT Optics

The science MOT is established in a so-called mirror-MOT setup, which has been introduced in [47, 48, 49]. As illustrated in Fig. 3.25, an atom chip with a gold layer surface is used as a mirror, reducing the solid angle required by the MOT beams. Similarly, the number of MOT beams is reduced to four beams, two counter-propagating horizontal beams and two beams, which have an incident angle of 45° to the surface of the chip. Each of the 45° beams is reflected into the path of another one, thereby becoming the missing 5th and 6th MOT beams. The important point for the trap to function is that the handness of circular polarisation of the two 45° beams changes upon reflection.

The magnetic quadrupole field is generated by the broad copper U wire, which is situated below the atom chip (see subsection 3.3.3). Due to symmetry reasons, it is desireable to have the surface of the atomchip orthogonal to the direction of gravity. Therefore, the quadrupole
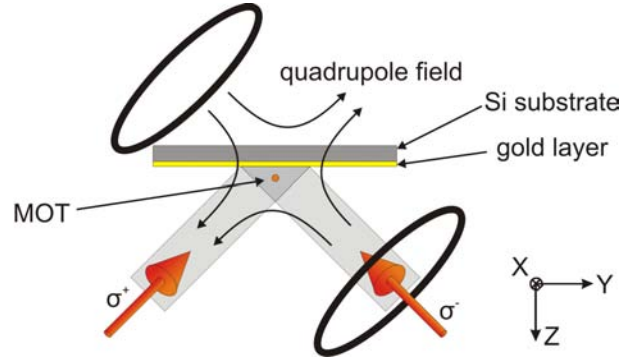
Figure 3.25: Mirror MOT scheme
The two 45° beams are reflected by the gold layer of the atomchip, reducing the solid angle required by the MOT beams. Upon reflection, the handness of the circular polarisation of the two beams changes. The two horizontal beams are perpendicular to the page and are not shown.

field is rotated by 45° by a homogeneous magnetic bias field, provided by the main bias coils (see section 3.4). Additionally, to be able to make time-of-flight measurements, the atom chip is facing down. The trapping potential of a BEC or thermal cloud is turned off. The sample can expand freely for some seconds and then be imaged. The imaged spatial distributions can be used to calculate the initial momentum distributions [50].

The optical components of the science mirror MOT are mounted on the two optics boards (see section 3.3.4 and Fig. 3.20). As can be seen in Fig. 3.26, the laser beam is split by the first PBS into two beams, one is used for the horizontal beams and the other one is sent through a hole in the optics board, that is 30mm in diameter, to one level below, to be used for the two 45° beams. The collimated laser beam after the outcoupler is approximately 14mm in diameter. Each MOT beam is expanded by a factor of 1.5 by a Galileian like telescope, just before it enters the steering stage of two two inch steering mirrors[41].

3.5.3 The Push Beam

A circularly polarized push beam is used to transfer ^{87}Rb and ^{40}K atoms from the collection MOT to the science MOT. They may be transferred separately, one species after the other, or

---
[41]all optic components supplied by Lens Optics GmbH
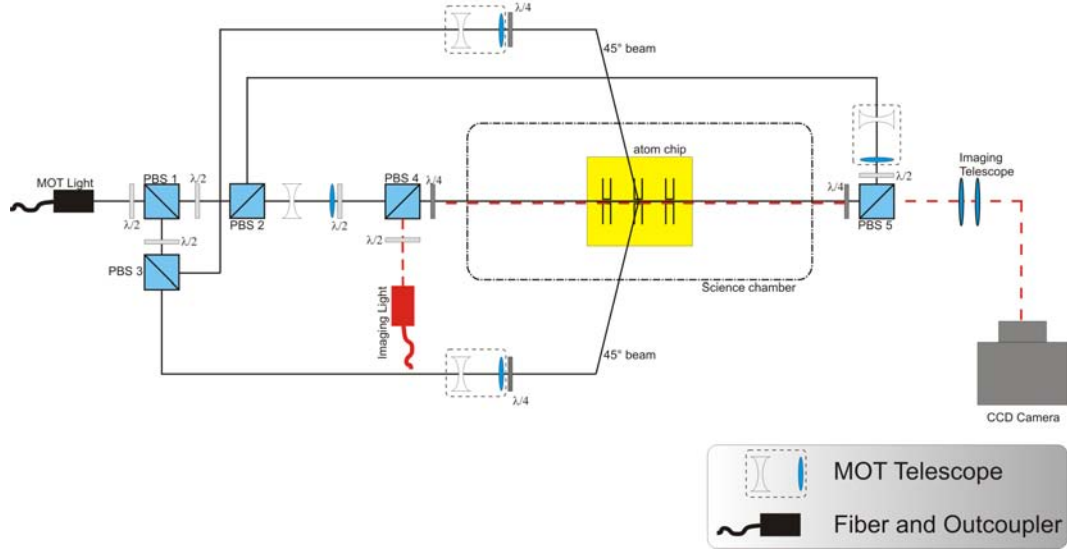
Figure 3.26: Mirror MOT optics scheme
The laser beam is split by PBS1 into two beams, one is used for the horizontal beams and the other one is sent through a hole of 30mm in diameter in the optics board one level below, to be used for the two 45° beams. Each MOT beam is expanded by a factor of 1.5 by a Galilei like telescope just before it enters a steering stage, omitted for clarity. Graphic based on [23].

both species at the same time. The science MOT is loaded via the push beam.

The axis of the push beam goes through the center of the collection chamber, the differential pumping stage, then hits the center of the chip where the push beam is reflected and finally leaves the science chamber on the other side through an DN16CF viewport.

Chapter 4

Collection MOT Measurements

4.1 Overview

This chapter describes how basic physical properties of ^{87}Rb and ^{40}K MOTs can be measured using a standard commercially available photodiode or a CCD camera, which both collect the fluorescence emitted by the MOT. Physical properties cover the number, density and temperature of trapped atoms in the MOT, the loading behaviour of the MOT and the optical density of the atom cloud. The applied methods and measurement setups will be discussed in detail. The dependence on various trapping parameters will be studied and optimal trapping parameters will be obtained. Such trapping parameters are the laser light intensity and frequency, the gradient of the quadrupole magnetic field of the MOT and the alkali dispenser currents.

The differences between physical properties concerning the trapping behaviour of ^{87}Rb and ^{40}K will be explained and in particular the hyperfine structure will be examined.

The outline of this chapter is as follows: First a single ^{87}Rb MOT is studied; and second, a single ^{40}K MOT is examined.

4.2 Single ^{87}Rb MOT in the Collection Chamber: Preliminary Results

4.2.1 Atom number

For the characterization and optimization of a magneto-optical trap (MOT), it is essential to characterize the variation in trapped atom number with the trapping parameters such as, for example, laser detuning, magnetic field gradient, and laser intensity.

Measuring the fluorescence emitted by the atoms is an easily applied method of gaining a rough estimate of the atom number, which is directly proportional to the fluorescence signal. Therefore, a small fraction of the scattered photons is collected by a converging lens at a (Caburn) Diameter Nominal 16mm Conflat DN16CF viewport of the vacuum chamber and imaged on a photodiode[1] (see Fig 4.1). The MOT can be treated as a point source, emitting light isotropically in 4π.

The number of atoms is derived by the following considerations:

- The atom number N is equal to the total emitted power in 4π over the emitted power per atom $E = h\nu$.

- The lens can only collect a fraction of the total emitted fluorescent radiation defined by the solid angle covered by the DN16CF viewport (see Fig. 4.1).

$$\eta_\Omega = \frac{r^2}{4d^2} = (2.5 \pm 0.2) \cdot 10^{-3} \tag{4.1}$$

- Some percentage of the light is lost due to reflection and absorption losses at the window and at the lens.

- The photodiode converts the absorbed power into a photodiode-current signal with an efficiency of approximately 0.53A/W[2] for 780nm. This current signal is again converted by a current amplifier[3] to a voltage signal, which can be displayed by a commercial

---

[1]ThorLabs DET 110, quoting g_{PD} from spec sheet
[2]ThorLabs DET 110, photodiode conversion efficiency as stated in spec sheet for 780nm
[3]Stanford Research Systems low-noise Current Amplifier Model SR570
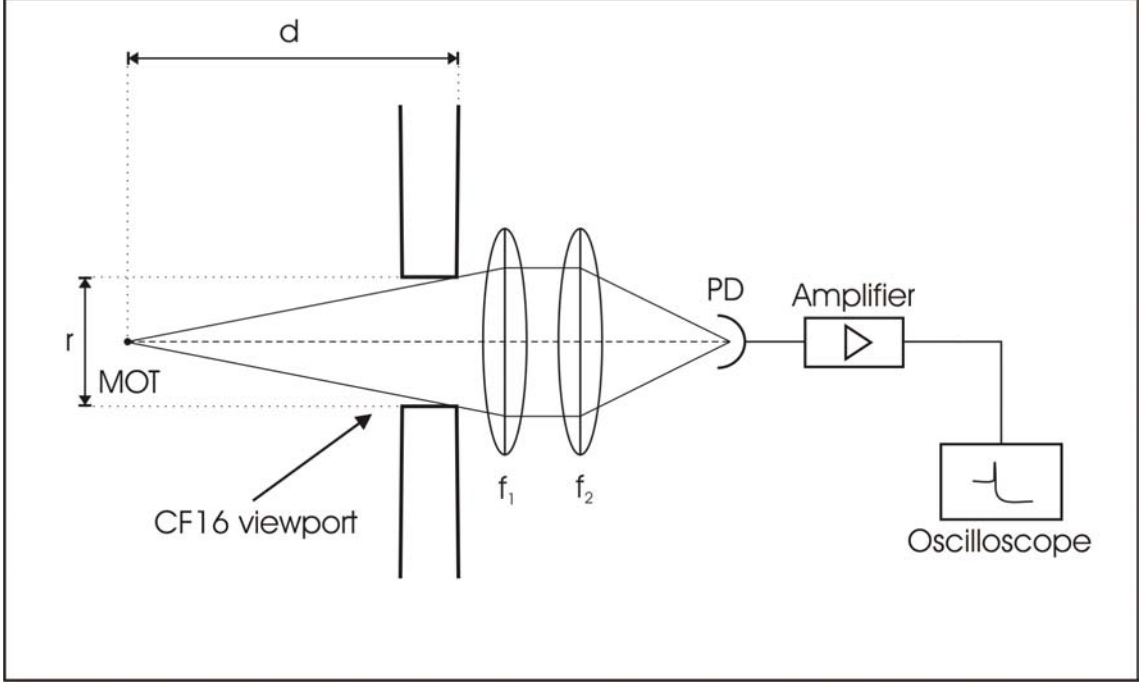
Figure 4.1: Detection scheme
A lens of suitable focal length f_1 is placed at a DN16CF viewport to collect the fluorescence emitted by the trapped atoms of the MOT. A second lens is used to focus the light on a photodiode[2]. The photodiode´s current signal is converted and amplified to a voltage signal[3], which can be displayed on a commercial oscilloscope. The collected solid angle is restricted by the radius r of the viewport and by the distance d between MOT and CF 16 outer surface.
$r = 8.0 \pm 0.1$mm, $d = 80 \pm 3$mm, $f_1 = 85$mm, $f_2 = 30$mm

oscilloscope or fed to an analogue channel of Adwin[4] for computerized data collection in real time and storage purposes. Therefore, the number of trapped atoms, N, in the MOT is calculated as in eq. 4.2.

$$N = \frac{I_{PD}}{g_{PD}\eta_\Omega\eta_{opt} \cdot h\nu R} = \frac{\Delta V \cdot g_{IV}}{g_{PD}\eta_\Omega\eta_{opt} \cdot h\nu R} \qquad (4.2)$$

where

---

[4]Jäger GmbH, http://www.adwin.de/

I_{PD} ...   photodiode current

ΔV ...   measured voltage difference (see Fig. 4.2)

R ...   scattering rate

g_{PD} ...   photodiode conversion efficiency $(0.53\text{A/W})^2$

g_{IV} ...   current-to-voltage converter gain (typically 50nA/V)

η_{opt} ...   optical efficiency (taking reflective losses into account)

η_{Ω} ...   solid angle collection fraction

For a two-level system the occupation probability of the excited state ρ_E can be derived by solving the static optical Bloch equations [11, 12, 10] which leads, with $R = \Gamma\rho_E$, to the following value of the scattering rate (see also section 2.1)

$$R = \frac{\Gamma}{2} \cdot \frac{I/I_{sat}}{1 + I/I_{sat} + 4\Delta^2/\Gamma^2} \tag{4.3}$$

with the natural linewidth (FWHM) $\Gamma = 2\pi \times 6.065(9)$MHz [15], the total cooling light intensity I, the saturation intensity for ^{87}Rb $I_{sat} = \pi hc/3\lambda^3\tau = 1.669$mW/cm^2 [15] (discussed below) and the detuning $\Delta = \omega - \omega_0$, where ω represents the cooling laser frequency and ω_0 the resonance frequency of the transition from the ground state to the excited state for the two-level atom; which in the case of ^{87}Rb is $F = 2 \rightarrow F' = 3$ of the ^{87}Rb D_2 line $(5^2S_{1/2} \rightarrow 5^2P_{3/2})$.

Two Different Procedures for Calculating the Scattering Rate R

There are now two methods of calculating the scattering rate R:

1. *Zero Laser Detuning:* The atoms are loaded into the MOT at a constant finite detuning until a steady state of the atom number is achieved. Then, the cooling beam frequency is ramped linearly in approximately 1ms from red detuning across resonance to blue detuning, hence removing the atoms from the trapping region. By crossing the atomic resonance a peak in the fluorescence signal and consequently a peak voltage signal ΔV is obtained as suggested by eq. 4.2. ΔV is defined by the maximum minus the background signal, as can be seen in Fig. 4.2. Further assuming that $I >> I_{sat}$ leads to $R \rightarrow \frac{\Gamma}{2}$. In our case, this assumption is justified, because the lowest total cooling laser intensity I used in our measurements equals 40 ± 2mW which leads to $I/I_{sat} \geq 23.4$. The rate
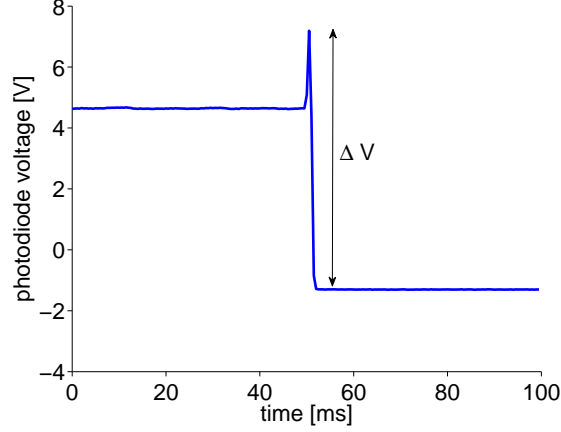
Figure 4.2: Photodiode signal

Typical atom number measurement for a total cooling light intensity of 90mW. Below 50ms the detuning δ is held constant at $-2\pi \times 19.84$MHz. The cooling beam frequency is then ramped linearly in 1ms to $+10.2$MHz. The further settings are: $I_{Dispenser} = 7.0 \pm 0.1$A; $\partial B / \partial z_{quad}^{center} = 8.0 \pm 0.4$G/cm; $I_{RbRepumper} = 15$mW. The derived mean atom number of three measurements using the same settings is $N = (7.3 \pm 0.2) \times 10^7$.

of spontaneous emission, which equals the scattering rate, from a two-level atom tends to $\frac{\Gamma}{2}$ (compare with eq. 4.3) for $I \gg I_{sat}$ because the populations in the excited and ground states both approach $\frac{1}{2}$. This can be seen directly from Einstein's rate equations for radiation interacting with a two-level atom [10]. This first method is used for all atom number determinations in this thesis, except for MOT loading measurements.

2. *Finite Laser Detuning:* This is a slightly more complicated approach due to the fact that quotes of the saturation intensity I_{sat} vary widely in the literature and each allowed transition has a separate saturation intensity. The total light field of the MOT stimulates all allowed near-resonant transitions. Therefore, if we assume an isotropic population distribution over the m_F levels and take the average I_S over all hyperfine $F = 2 \rightarrow F' = 3$ transitions, $I_{sat} = 3.49$mW/cm^2 [51], which does not agree with experimental results [51]. The average I_{sat} is now rarely used and the saturation intensity of the strongest atomic transition is commonly employed. All MOT number calculations in this thesis use the saturation intensity of the stretched state transition, which is $I_{sat(m_F = \pm 2 \rightarrow m_{F'} = \pm 3)} = 1.669(2)$mW/cm^2

[15] for ^{87}Rb and $I_{sat(m_F=\pm 9/2 \rightarrow m_{F'}=\pm 11/2)}$ =1.796mW/cm^2 [16] for ^{40}K. To measure the loading behavior of the MOT, this second method has been applied using the proper formula for R.

Comparing the resulting values of the two different methods for the same measurement data leads to agreement within approximately 3%.

Some words on the errors

The intensity loss of the collected scattered photons due to the vacuum window has been evaluated by direct measurement to be $12\% \pm 1\%$ and the intensity loss due to the lens itself has been evaluated to be $2.3 \pm 0.5\%$, leading to $\eta_{opt} = 0.86 \pm 0.01$.

The estimated absolute error of the atom number measurement is approximately 20% (calculated using eq. 4.4) and provides information of the magnitude of the atom number. The relative error in comparative measurements is estimated as 6%.

$$
\begin{aligned}
\triangle N &= \left(\left| \frac{\partial N}{\partial \eta_\Omega} \right|^2 (\triangle \eta_\Omega)^2 + \left| \frac{\partial N}{\partial \eta_{opt}} \right|^2 (\triangle \eta_{opt})^2 + \right. \\
&+ \left. \left| \frac{\partial N}{\partial (\triangle U)} \right|^2 (\triangle (\triangle U))^2 + \left| \frac{\partial N}{\partial R} \right|^2 (\triangle R)^2 + \left| \frac{\partial N}{\partial g_{PD}} \right|^2 (\triangle g_{PD})^2 \right)^{1/2}
\end{aligned}
\tag{4.4}
$$

Note: The error bars of the atom numbers displayed in the figures in this chapter indicate the statistical errors derived from one standard deviation[5] *of at least three measurements.*

The main sources of error are as follows:

systematic errors:

- solid angle (the estimated value has an error of 8%, see eq. 4.1)

- measurement error of the intensity loss due to lens (0.5%) and window (1%)

---

[5] $\sigma = \sqrt[2]{\frac{1}{n-1} \sum_{i=1}^{n} (\overline{x} - x_i)}$

- inexactness of the estimation that $I/I_{sat} \gg 1$ and that, therefore, I/I_{sat} cancels out of eq. 4.3

- inaccuracy of g_{PD} of 14%

- for only the finite laser detuning method discussed above:

    - error in the AOM voltage-frequency calibration

    - inaccuracy of I_{sat}

random errors:

- fluctuations in the laser intensity and laser frequency over time

- small variations in beam polarization after the out-coupler of the optical fibre, delivering the light to the MOT setup $\rightarrow$ variation in the power balance of the six MOT beams

- small changes in trap position, due to realignment of the MOT laser beams at the start of each measurement run, in order to obtain an as good as possible intersection of the laser beams. The intersection point position in space is therefore not exactly reproducible (the estimated upper bound of the error of the distance of the DN16CF viewport to the MOT is $\Delta d = \pm 3$mm)

Reabsorption processes of scattered photons inside the atom cloud are completely ignored here. The effect of an optical dense atom cloud is discussed in detail in [52, 53].

4.2.2 Detuning of the Cooling Laser Light for Number Measurements

The trapped atom number is strongly dependent on the detuning of the ^{87}Rb cooling laser, which is locked to the $F' = 1/F' = 3$ crossover of the transition $F = 2 \rightarrow F'$ of the D_2 line $(5^2S_{1/2} \rightarrow 5^2P_{3/2})$. In order to determine the number of trapped atoms in the MOT, the *Zero Laser Detuning Method,* as discussed in section 4.2.1, is applied. The lockpoint of the cooling laser is the 1-3 crossover in Fig.3.5, comparing with 3.4, the detuning Δ is given by

$$\triangle[MHz] = -212.15 + 2 * f_{AOM}[MHz]. \tag{4.5}$$

Fig. 4.3 illustrates the dependence of the atom number on the detuning of the ^{87}Rb cooling laser for the following settings: $I_{Dispenser} = 7.0 \pm 0.1$A, $I_{Quadrupole} = 2 \pm 0.1$A, $I_{RbRepumper} = 15 \pm 1$mW/cm^2, $I_{RbCooler} = 90 \pm 1$mW/cm^2 with the maximum atom number at $\Delta = -19.84$MHz. Fig. 4.4 shows a plot for the same settings but for all applied beam intensities. The atom number has a maximum of $(7.3 \pm 0.2) \times 10^7$ (one standard deviation) for the same detuning of -19.84MHz and a total cooling light intensity of approximately 94.5mW/cm^2

Owing to the fact that the AOM frequency shifting effects slightly the incoupling of the cooling beam into the optical fibre, the output beam intensities change for different detunings. An intensity adjustment factor for each applied detuning is obtained by measurement. This adjustment leads to the white spaces and "skewed features" in Fig. 4.4.
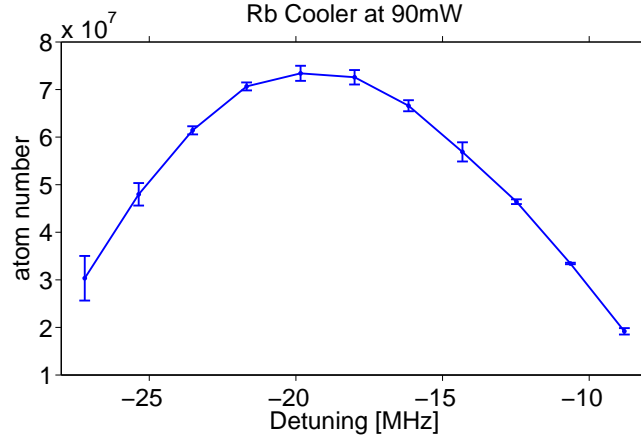
Figure 4.3: Variation of atom number with the detuning of the ^{87}Rb cooling laser. Each point represents the average of 3 measurements. The vertical error bars are given by one standard deviation. The following settings have been used: $I_{Dispenser}^{Rb} = 7.0 \pm 0.1$A, $\partial B/\partial z_{quad}^{center} = 8.0 \pm 0.4$G/cm, $I_{Repumper}^{Rb} = 15.0 \pm 0.5$mW/cm^2. A maximum of $(7.3 \pm 0.2) \times 10^7$ (one standard deviation) trapped atoms is found for a total detuning of -19.84MHz and cooling laser beam intensity of approximately 94.5mW/cm^2

4.2.3 Loading Behaviour

The trapped atoms in the preparation MOT are transferred by a push beam through a differential pumping tube to the science mirror MOT. Therefore, the loading rate of the 3D preparation MOT and the maximum available atom flux are important parameters for the experiment.
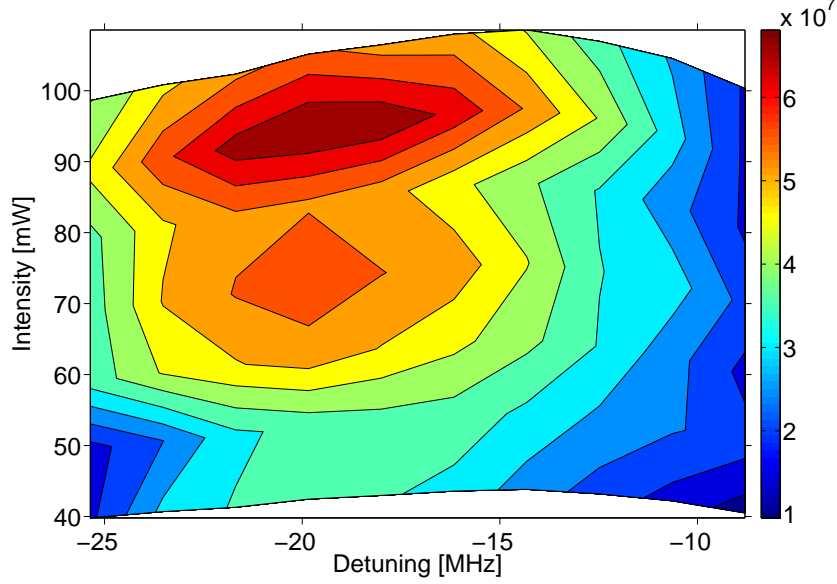
Figure 4.4: Finding optimal trap parameters

Atom number dependence on the intensity and detuning of the ^{87}Rb cooling laser measured with the following settings: $I_{Dispenser}^{Rb} = 7.0 \pm 0.1$A, $\partial B/\partial z_{quad}^{center} = 8.0 \pm 0.4$G/cm, $I_{Repumper}^{Rb} = 15.0 \pm 0.5$mW/cm^2. A maximum of $(7.3 \pm 0.2) \times 10^7$ (one standard deviation) trapped atoms is found for a detuning of -19.84MHz and a total cooling beam intensity of approximately 94.5mW/cm^2

The atoms are loaded into the MOT at a loading rate L. This rate depends on the size of the trapping region, laser beam intensity and detuning, the quadrupole magnetic field and the ^{87}Rb partial pressure. The loss processes include losses due to interspecies collisions and collisions with the background gas. The rate equation for the trapped atom number is [54]

$$\frac{dN}{dt} = L - N\underbrace{\left(\frac{1}{\tau_{Rb}} + \frac{1}{\tau_{bg}}\right)}_{\frac{1}{\tau_{MOT}}} \quad - \quad \underbrace{\beta \int n^2 dV}_{density\ dependent\ losses} \tag{4.6}$$

where
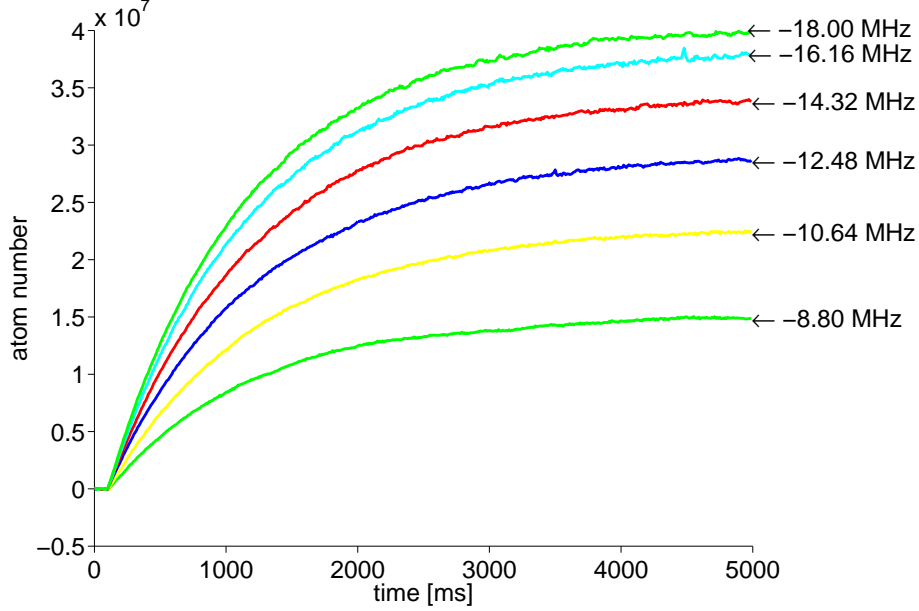
Figure 4.5: MOT loading curves

Loading curves for various (linear) detunings (labeled) are shown for a beam intensity of approximately 20mW/cm^2 and $I_{Dispenser}^{Rb} = 7.0 \pm 0.1\text{A}$, $\partial B/\partial z_{quad}^{center} = 8.0 \pm 0.4\text{G/cm}$, $I_{Repumper}^{Rb} \cong 15.0 \pm 0.5\text{mW/cm}^2$. Atom numbers were determined using the second method discussed in section 4.2.1

$1/\tau_{bg}$	...	trap loss rate due to collisions with the background gas
$1/\tau_{Rb}$	...	loss rate due to interspecies collisions
τ_{MOT}	...	MOT loading time
β	...	loss coefficient for density dependent losses
L	...	loading rate

In the regime of low MOT densities, density-dependent losses can be neglected ($\beta = 0$) and the rate equation becomes

$$\frac{dN}{dt} = L - N\frac{1}{\tau_{MOT}}, \tag{4.7}$$

which yields the solution

$$N(t) = N_\infty \cdot \left(1 - e^{-\frac{t}{\tau_{MOT}}}\right) \tag{4.8}$$

for the boundary condition of $N(0) = 0$ and the steady-state condition $\frac{dN}{dt} = 0$, where $N_\infty =$

$L \cdot \tau_{MOT}$, the value of the maximum trapped atom number.

In Fig. 4.6, a non-linear least-squares fit using the Levenberg-Marquard algorithm [55, 56] has been applied. This leads to the following fitting parameter values[6]:

$$
\begin{aligned}
N_\infty &= (5.079 \pm 0.007) \cdot 10^7 \text{ atoms} \\
\tau_{MOT} &= 1082 \pm 2\text{ms} \\
L &= (4.612 \pm 0.006) \cdot 10^7 \text{atoms/sec} \\
RMSE^6 &= 1.531 \cdot 10^5 \text{ atoms}
\end{aligned}
$$

Comparing our loading rate with similar experiments of our group [57, 58], leads to the conclusion that the loading rate should still be increased by a factor of at least 10.
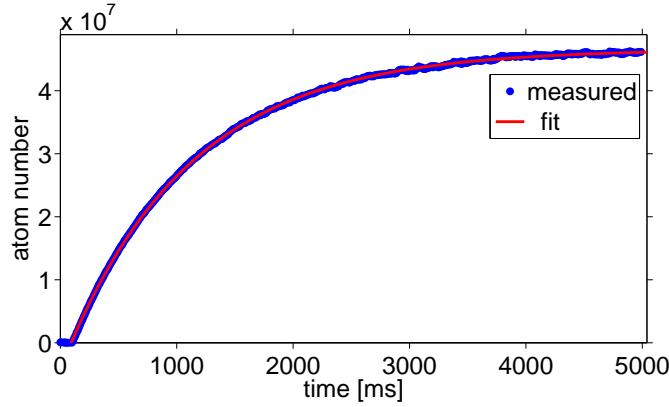
Figure 4.6: Loading curve fit

Loading curve fitted with a non-linear least-squares fit using the Levenberg-Marquard algorithm. The atom number was determined using the second method discussed in 4.2.1. The following parameters have been used: $\Delta = -18.0 \pm 0.5$MHz, $I^{Rb}_{Cooler} = 60 \pm 1$mW/cm^2, $I^{Rb}_{Repumper} = 15 \pm 1$mW/cm^2, $\partial B/\partial z^{center}_{quad} = 8.0 \pm 0.4$G/cm, $I_{Dispensers} = 7.0 \pm 0.1$A

---

[6]root-mean-squared error $RMSE = \sqrt[2]{\frac{\sum_{i=1}^{n} res(i)^2}{n}}$ *with the residual* $res(i) = originaldata(i) - fitteddata(i)$
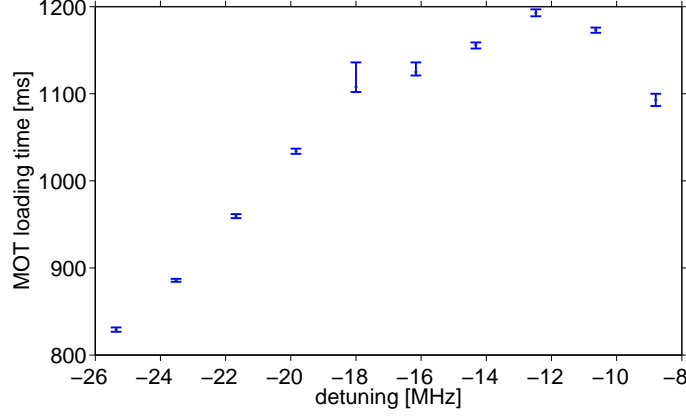
Figure 4.7: Dependence of loading time on the detuning

Derived MOT loading times from several non-linear-least-squares fits illustrated in figure 4.6 for different detunings of the ^{87}Rb cooling laser for the following setting: $I_{Cooler} = 60 \pm 1\text{mW/cm}^2$, $I_{Repumper} = 15.0 \pm 0.5\text{mW/cm}^2$, $\partial B/\partial z_{quad}^{center} = 8.0 \pm 0.4\text{G/cm}$, $I_{Dispensers} = 7.0 \pm 0.1\text{A}$

4.3   Single ^{40}K MOT in the Collection Chamber: Preliminary Results

4.3.1   Potassium is different

In figure 4.8 the hyperfine structure of ^{87}Rb, ^{39}K and ^{40}K are compared. As can be seen, the level structure for the two bosons ^{87}Rb and ^{39}K is very similar since both have a nuclear spin of $I = 3/2$ and the selection rules for the D_2 line between the four excited states and the two ground states are identical. In conclusion the same hyperfine transitions are allowed.

On the contrary, the hyperfine structure of the fermion ^{40}K is different, because both the excited states and ground states are inverted (see figure 4.8) [59, 60]. This complete inversion is caused by a large nuclear spin of I=4 that points in the opposite direction to the nuclear magnetic moment, resulting in a negative dipole moment. As can be seen in figure 4.8, the separation between excited states is relatively small compared to rubidium and the ground states are only separated by approximately 1 GHz.

In alkalis with large ground-state hyperfine splittings, such as rubidium and cesium, optical pumping (see spectroscopy part of subsection 3.2.2) is easily compensated using a weak (in
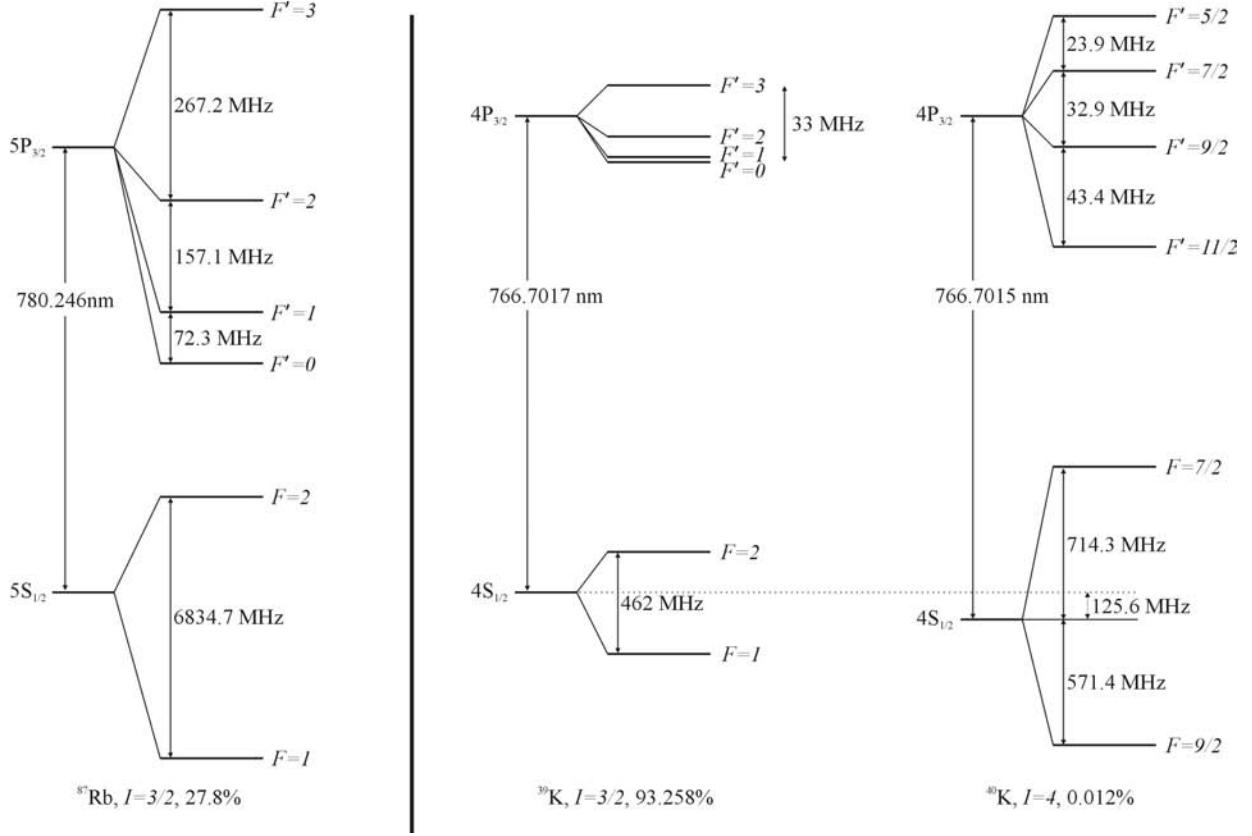
Figure 4.8: Hyperfine structure of ^{87}Rb, ^{39}K and ^{40}K

Energies of ^{87}Rb, ^{39}K and ^{40}K hyperfine levels in the $4S_{1/2}$ and $4P_{3/2}$ terms (D_2-line). The natural abundances of each isotope are given. Data adapted from [59, 60, 15].

power) repumping laser, since off-resonant terms give a transition probability which is some orders of magnitude smaller than the resonant term. The atom can be treated as a two-level system with an excited-state population given by (compare with section 2.1.1)

$$\rho_E^{(2)} = \frac{1}{2} \left(\frac{I_{tot}/I_{sat}}{1 + I_{tot}/I_{sat} + 4\left(\Delta/\Gamma\right)^2} \right), \tag{4.9}$$

which is direct proportional to the scattering force $\vec{F}_{scatt} = \hbar\vec{k} \cdot R$ with the scattering rate $R = \Gamma\rho_E^{(2)}$. Here again Δ corresponds to the detuning of the cooling laser from the $S_{1/2}(F = I + 1/2) \rightarrow P_{3/2}(F' = I + 3/2)$ transition, I_{tot} is the total trapping laser intensity and

I_{sat} is the saturation intensity.

For both potassium isotopes considered here, optical pumping is very strong due to the tight hyperfine level spacing of the excited states in the $P_{3/2}$ term. A fast depletion of the $F = 2$ ground state towards the $F = 1$ state results in the necessity of a relatively strong repumping light intensity comparable to that of the cooling laser intensity. This results in the fact that a cooling force arises from both frequencies. It does not make any more sense to speak of cooling and repumping light, apart from sticking to a wide spread convention. The actual hyperfine structure may therefore not be omitted in the calculations of the excited-state population ρ_E, which in turn influences the calculation of the atom number.

This very different behaviour of potassium makes its cooling more difficult and more dependent on fine frequency tuning than rubidium [61].

Furthermore, it should be noted, that the level spacing of the bosonic potassium isotopes is so small that these lines cannot be distinguished by means of ordinary absorption spectroscopy [62] (compare with Fig. 3.11).

Some more words on the two-level excited-state population $\rho_e^{(2)}$. As can be seen in eq. 4.9, $\rho_e^{(2)}$ depends strongly on the total trapping laser intensity I_{tot}. For $I_{tot} > I_{sat}$ the atomic transition can be saturated and $\rho_e^{(2)}$ reaches the maximum value of 0.5. For even higher trapping intensities, the transition is saturated at zero detuning, whereas for $\Delta \neq 0$ the absorption can still increase. Therefore, a broadening of the linewidth can be observed, which is known as *power broadening*. Fig. shows the two-level excited-state population fraction for different fractions of I_{tot}/I_{sat} in dependence of the detuning Δ.

4.3.2 Six-level Model

As described in section 4.3.1 above, potassium atoms may not be treated as a two-level system like the rubidium atoms were in section 4.2.1. Therefore, in equation 4.2 the scattering rate R, valid only for a two-level system, has to be exchanged with the total excited-states population fraction generated by the laser radiation of the MOT trapping beams acting on a six-level system. Thus, to determine the atom number of a ^{40}K MOT, the total excited-states population fraction $\rho_E^{(6)}$ has to be calculated. In the following, a simple six-level model simulating the hyperfine structure of ^{40}K is discussed. It was first described by Williamson [59] and was
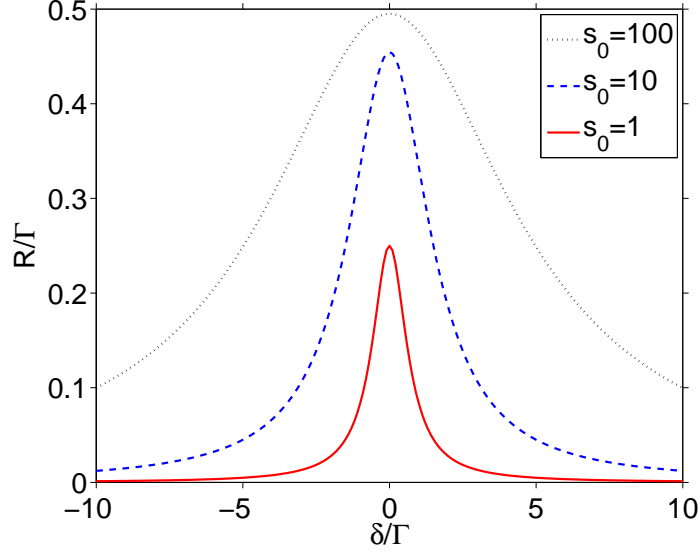
Figure 4.9: Power broadening of the two-level excited-state population fraction $\rho_e^{(2)}$ plotted versus the detuning Δ over the natural linewidth Γ for different values of the saturation parameter $s_0 = I_{tot}/I_{sat}$. For big values of s_0 power broadening can be observed.

inspired by a model of Lindquist et al. [63] and a model by Gibble et al. [64].
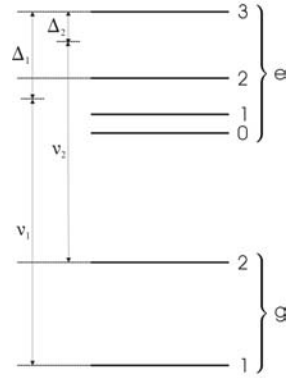
Figure 4.10: Visualization of a six-level system

Definitions of the laser detunings and hyperfine levels in the six-level model. The numeric labels correspond to $I = 3/2$. For ^{40}K the hyperfine levels are inverted, meaning that levels of higher m_f values lie lower in energy.

The six levels consist of two ground states and four excited states, illustrated in figure 4.10 on the previous page. The atom is illuminated by two lasers. The repumping laser of frequency ν_1, detuning $\triangle_1$ and intensity I_1 and the cooling laser of frequency ν_2, detuning Δ_2 and intensity I_2. Typically, red detunings ($\triangle < 0$MHz) are used. The population of each hyperfine level is allowed to change over time, assuming, initially, equally occupied Zeeman sublevels within each hyperfine state. Optical coherences are ignored and a simple rate equation ansatz is made.

For each excited-state population p_e ($e = a, b, c, d$), the rate equation is given by

$$\dot{p}_e = R_{e1}(p_1 - p_e) + R_{e2}(p_2 - p_e) - \Gamma p_e \tag{4.10}$$

where p_1 and p_2 are the two ground state populations. R_{eg} is the excitation rate between the excited state e and ground state g with $g = 1, 2$. $\tau = 2\pi/\Gamma = 27.05$ [16] is the lifetime of the $P_{3/2}$ level.

The ground state populations are given by [59]

$$\dot{p}_g = \sum_e [R_{eg}(p_e - p_g) + \Gamma_{eg}p_e] \tag{4.11}$$

where Γ_{eg} is defined using the branching ratio b_{eg} from e to g as $\Gamma_{eg} = b_{eg}\Gamma$ and fulfills the relation $\Gamma = \Gamma_{e1} + \Gamma_{e2}$.

The excitation rates are given by [59]

$$R_{eg} = \frac{c_{eg}\Gamma_{eg}}{2}\left(\frac{I_g/I_{sat}}{1 + 4\left(\frac{\nu_g - \nu_{eg}}{\Gamma}\right)^2}\right). \tag{4.12}$$

I_g and ν_g are the laser intensity and frequency corresponding to ground level g. The coefficients c_{eg} are the oscillator strengths, which are averaged over individual Zeeman levels of the m_F manifold and over polarizations. c_{eg} are then normalized over the sum over all levels. ν_{eg} are the atomic transition frequencies. The saturation intensity of the D_2 line[7] of potassium is $I_{Sat} = 1.796$mW/cm^2 [65, 16].

In steady state, $\dot{p}_e = \dot{p}_g = 0$, where excitation and emission rates for each state are equalized, we obtain for the excited-state population

---

[7]for the following transition: $^{40}K : |4^2S_{1/2}, F = 9/2, m_F = \pm9/2\rangle \longleftrightarrow |4^2P_{3/2}, F = 11/2, m_F = \pm11/2\rangle$

$$p_e = \frac{R_{e1}p_1 + R_{e2}p_2}{R_{e1} + R_{e2} + \Gamma} \tag{4.13}$$

and for the ground-state population

$$p_g = \frac{\sum_e (R_{eg} + \Gamma_{eg}) p_e}{\sum_e R_{eg}}. \tag{4.14}$$

Combining equations 4.13 and 4.14 leads to

$$p_g = \frac{\sum_e \frac{(R_{eg} + \Gamma_{eg})(R_{e1}p_1 + R_{e2}p_2)}{R_{e1} + R_{e2} + \Gamma}}{\sum_e R_{eg}} \tag{4.15}$$

and p_2 can be written in terms of p_1 as:

$$p_2 = \frac{\sum \frac{R_{e2} + \Gamma_{e2}}{R_{e1} + R_{e2} + \Gamma} R_{e1}}{\sum \frac{R_{e1} + \Gamma_{e1}}{R_{e1} + R_{e2} + \Gamma} R_{e2}} p_1 \tag{4.16}$$

This equation can be solved by iteration. First assigning p_1 an arbitrary value of $p_1 = 1$, calculating p_2, then calculating the four p_e using equation 4.13 and finally summing the results for all six levels in order to retrieve a normalization factor with which all populations are divided, so that in the end the resulting populations fulfill the following criteria:

$$\sum_g p_g + \sum_e p_e = 1 \tag{4.17}$$

The total excited-state population fraction is then simply calculated as

$$\rho_E = \sum_e p_e. \tag{4.18}$$

4.3.3 Numerical Comparison between two-level and six-level excited-states population fraction

Of course, the question arises as to whether the values of ϱ_E calculated using the two models are significantly different and hence result in a significantly different calculated atom numbers for a ^{40}K MOT. This subsection investigates this question numerically.
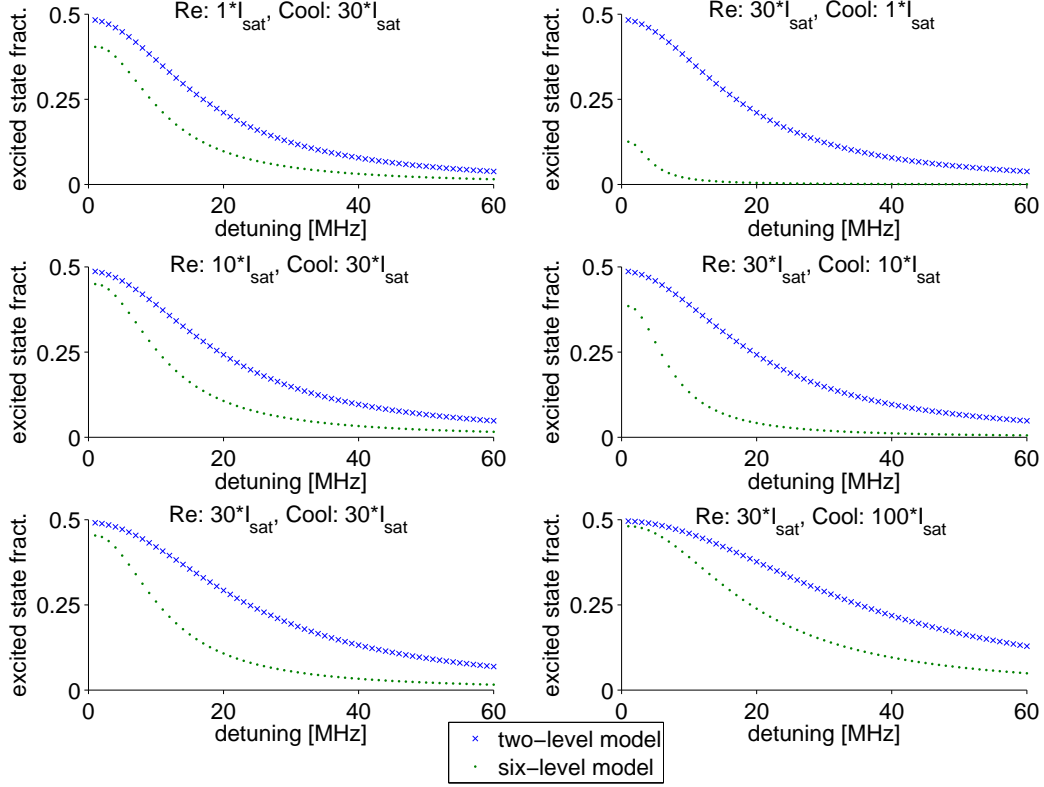
Figure 4.11: ^{40}K excited-state population fraction

Calculated with simple multilevel model (green) and with two-level approach (blue). The absolute value of the negative detuning of the cooling laser light is plotted. *left:* To understand the role of the repumping beam, the cooling beam intensity I_{Cool} is fixed and the repumping beam intensity I_{Re} is increased. *right:* To show the effect of weak cooling beams $I_{Re} = constant$ and I_{Cool} is varied.

A Matlab[8] program, which executes the calculations given in the previous section 4.3.2, has been developed. The results are shown graphically in figure 4.11 to 4.14. The blue curves show the excited-states population given by the two-level model (eq. 4.9) and the green curves illustrate the excited-states population calculated using the six-level model. The graphs plotted in the left part of figure 4.11 demonstrate the influence of the repumping light power on ρ_E, cooling light intensity is set constant and repumping light intensity is varied. Only for small

---

[8]R2007a, copyright by the MathWorks, Inc.

detunings of the cooling laser light and almost equal powers of repumping and cooling light (bottom left graph) does the six-level model $\rho_E^{(6)}$ deliver values for ϱ_E compareable to the two-level model $\rho_E^{(2)}$ with $\rho_E^{(6)} (\Delta = 0 MHz) = 0.4535$ and $\rho_E^{(2)} (\Delta = 0 MHz) = 0.4839$. Δ refers here always to the detuning of the cooling laser beam. The repumping laser light is set to zero detuning with respect to the transition frequency. On the right hand side of figure 4.11 are graphs for when the cooling light power is increased and the repumping intensity is held constant. For a weak cooling beam ($I_{Cool} = 1/30 \cdot I_{Re}$) almost no excitation is produced. The strong repumping beam excites the atoms in the $F' = 9/2$ state, which may decay spontaneously into both ground states $F = 9/2, 7/2$. Too few atoms in the $F = 9/2$ state are excited by the weak cooling beam. In steady state, the majority of the atoms (87.41%) occupy the $F = 9/2$ ground state and $\rho_E^{(6)} (\Delta = 0 MHz) = 0.1253$. For $I_{Cool} = 1/10 \cdot I_{Re}$ this effect is compensated slightly with $\rho_E^{(6)} (\Delta = 0 MHz) = 0.3847$. For all illustrated ratios of cooling and repumping intensity, $\rho_E^{(2)}$ is practically unimpressed.

Figure 4.12 illustrates again the great importance of a strong repumping beam for ^{40}K, contrary to figure 4.13 for ^{87}Rb. Compared to the six-level model calculated $\rho_E^{(6)}$ the error in the atom number obtained by the approximation of $\rho_E = 0.5$ is at least 6.2%.

	$I_{Re}/I_{Cool} = \frac{1}{100}$	$I_{Re}/I_{Cool} = \frac{1}{10}$
$\rho_E^{(2)}$	0.4951	0.4955
$\rho_E^{(6)}$	0.3531	0.4689

Table 4.1: ^{40}K values of ρ_E corresponding to figure 4.12

Figure 4.13 illustrates that for ^{87}Rb, weak repumping beam powers ($1/100 \cdot I_{Cool}$) are sufficient to obtain practically equal excited-states population as for a two-level system ($\rho_E^{(6)} (\Delta = 0) = 0.4910$, $\rho_E^{(2)} (\Delta = 0) = 0.4951$). As can be seen, nothing is gained by increasing I_{Re}. In conclusion, in a setup of a cooling and a weak repumping beam, treating ^{87}Rb as a two-level system is satisfactory. Compared to the six-level model the resulting error by approximating ρ_E as 0.5 in the atom number calculation is less than 2%.

By increasing the detuning of the cooling laser light of ^{87}Rb further than -267.2MHz, the $F' = 2$ level is crossed and for $\Delta = -424.3$MHz the $F' = 1$ level becomes resonant. This obviously results in a peak of the excited-states population fraction which is shown in figure 4.14.
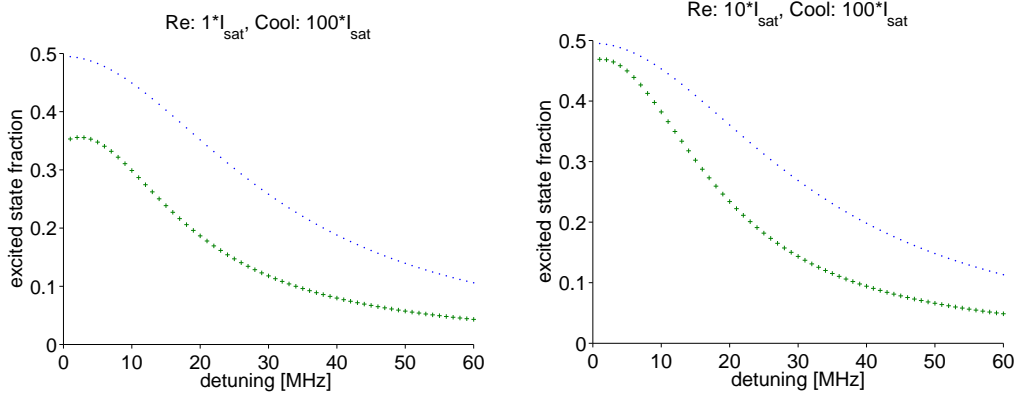
Figure 4.12: ^{40}K excited-state population fraction
Calculated with simple multilevel model (green crosses) and with two-level approach (blue dots). The absolute value of the negative detuning of the cooling laser light is plotted. The repumping beam is not detuned. I_{Cool} is held constant whereas I_{Re} is increased. To produce a two-level system like behaviour of $\rho_E^{(6)}$ a strong repumping beam is needed.
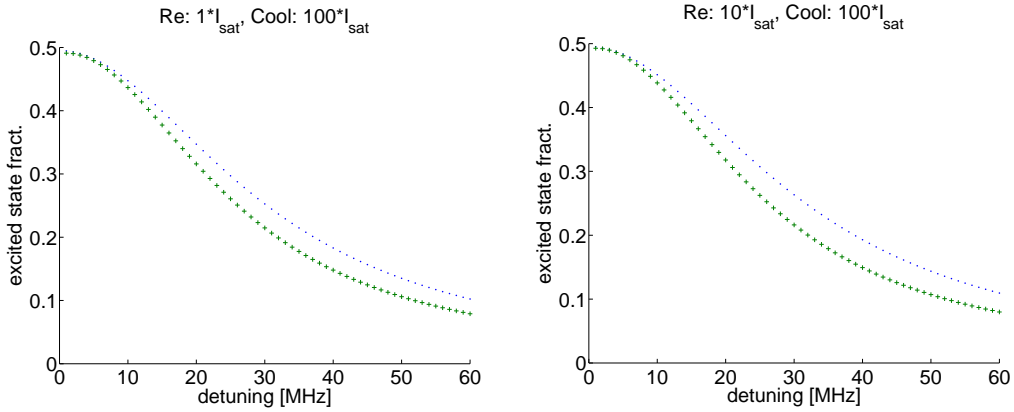
Figure 4.13: ^{87}Rb excited-state population fraction
Calculated with simple multilevel model (green crosses) and with two-level approach (blue dots). The absolute value of the negative detuning of the cooling laser light is plotted. The repumping beam is not detuned. As in figure 4.12, I_{Cool} is held constant whereas I_{Re} is increased. For ^{87}Rb, an I_{Re} equal to 1% of I_{Cool} is already sufficient to obtain a two-level system behaviour of $\rho_E^{(6)}$.

As ^{40}K exhibits an inverted hyperfine structure as discussed in section 4.3.1, the $F = 11/2$ state, used for cooling, has the lowest energy of the $P_{3/2}$ manifold. Increasing the absolute
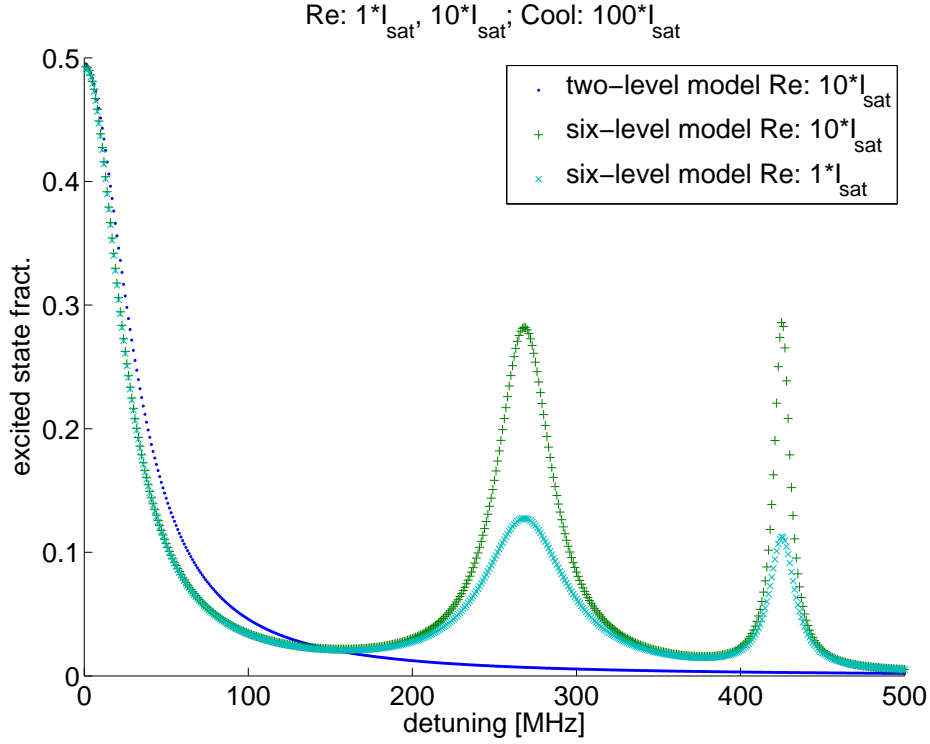
Figure 4.14: ^{87}Rb excited-state population fraction
Calculated with simple multilevel model (green and turquoise crosses) and with two-level approach (blue dots). The absolute value of the negative detuning of the cooling laser light is plotted. The repumping beam is not detuned. The detuning of the cooling light is varied over a wide range to cross the resonances of the $F = 2 \rightarrow F' = 2, 1$ transitions. The zero detuning point is the cooling transition $F = 2 \rightarrow F' = 3$.

value of the negative detuning does not result in the crossing of another hyperfine transition.

4.3.4   Atom Number Determination of ^{40}K

To determine the trapped atom number in a ^{40}K MOT, the same procedures as already described for ^{87}Rb in section 4.2.1 are used[9]. To calculate the atom number the *Zero Laser Detuning Method* is applied, to record the loading behaviour of the MOT the *Finite Laser Detuning Method* is used.

---

[9]ThorLabs DET 110, quoting g_{PD} from spec sheet

By using the results obtained in the previous section one obtains, in contrast to equation 4.2, for the ^{40}K atom number in a MOT:

$$N = \frac{\Delta V \cdot g_{IV} \cdot \tau}{g_{PD}\eta_\Omega\eta_{Opt} \cdot h\nu\rho_E} \tag{4.19}$$

where

τ	...	excited state life time
ΔV	...	measured voltage difference (see Fig. 4.2)
ρ_E	...	excited-state population fraction
g_{PD}	...	photodiode conversion efficiency (0.49A/W)[9]
g_{IV}	...	current-to-voltage converter gain (typically 10nA/V)
η_{Opt}	...	optical efficiency (taking reflective losses into account)
η_Ω	...	solid angle collection fraction

4.3.5 Obtained Atom Number for different Detunings

Like Fig. 4.3 for ^{87}Rb, Fig. 4.15 shows the dependence of the number of trapped ^{40}K atoms on the detuning of the potassium cooling beam frequency. The optimal detuning seems to ba at -44.0 ± 0.5MHz, where $(1.34 \pm 0.01) \times 10^6$ ^{40}K atoms are trapped.

4.3.6 Variation of the Dispenser Current

Before connecting the collection chamber with the science chamber the home-built potassium dispensers had to be tested. The dependence of the trapped-atom number on the dispenser current is illustrated in Fig. 4.16.

Only a slight increase in the atom number can be observed between 4A and 6.5A, which can be explained by a heating and degassing of K atoms which have been left behind from previous heatings and stuck on the surface of the dispensers. 7A seem to be the threshold current for the actual operation of the potassium dispensers, triggering the reduction reaction of eq. 3.11 discussed in subsection 3.3.2. Setting the current back to 4A stops the reduction process immediately, as can be seen by the fast decrease in Fig. 4.16.
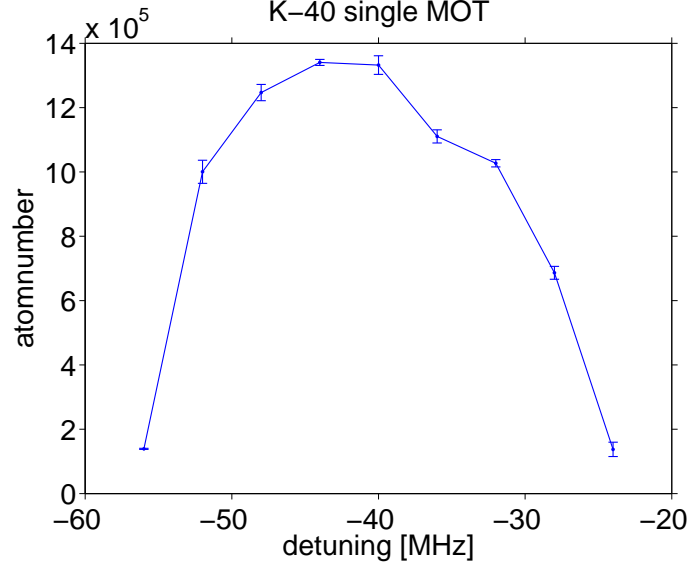
Figure 4.15: Atom number in dependence of repumper detuning

The following settings have been used: $I_{Dispenser}^{K} = 7.0 \pm 0.1$A, $\partial B/\partial z_{quad}^{center} = 16.2 \pm 0.4$G/cm, $I_{Repumper}^{K} = 25 \pm 1$mW/cm^2. A maximum of $(1.34 \pm 0.01) \times 10^6$ (one standard deviation) trapped atoms is found for a total detuning of -44.0 ± 0.5MHz and cooling laser beam intensity of approximately 80 ± 5mW/cm^2. Line, connecting the data points, is a guide for the eye.

4.3.7 Effect of MOT Magnetic Field Gradient on the Number of Trapped Atoms

As explained in section 2.2.1, the magnetic field gradient of the quadrupole field generated by two coils in anti-Helmholtz configuration, provides the spatially dependent scattering force, necessary to form an atom trap. In Fig. 4.17 the atom number is plotted against the gradient of the strong axis[10] of the magnetic field at the trap center. The bigger the gradient, the more atoms can be trapped, until the density in the MOT increases into the regime, where density dependent losses prevent further trapping (see eq. 4.6).

---

[10]symmetry axis of the coils
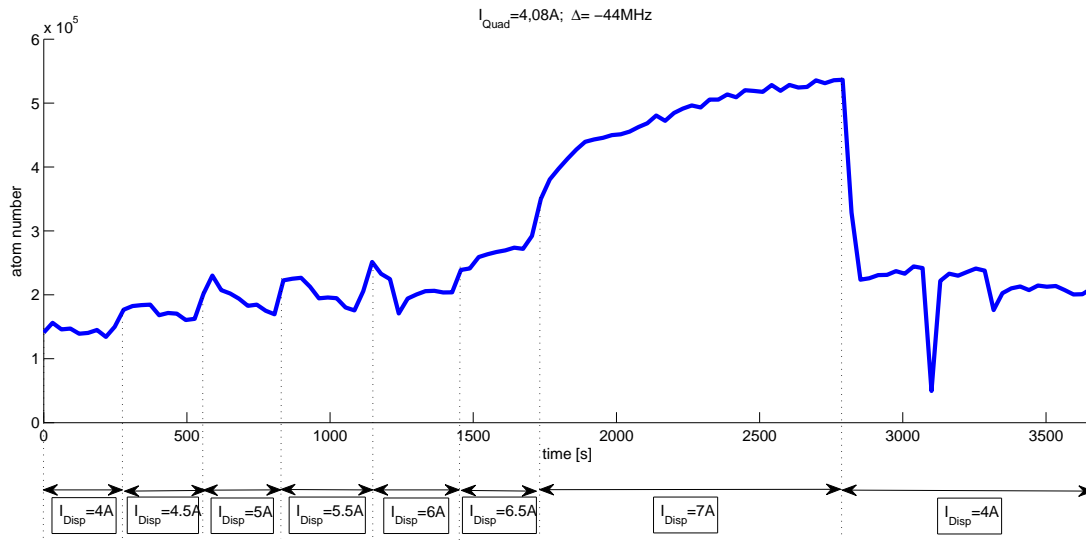
Figure 4.16: Atom number variation in dependence of dispenser current
The threshold current that triggers the reduction process in the potassium dispensers, thereby
emitting potassium atoms into the vacuum, is found to be at approximately 7A. For a current
below 7A, only potassium atoms sticking to the surface of the dispensers are degassed. Setting
the current from 7A back to 4A stops the reduction process immediately.

Figure 4.17: Dependence of ^{40}K atom number on magnetic field gradient
The magnetic field gradient in the direction of the strong axis (symmetry axis of the coils) of the quadrupole field is plotted. The detuning of the cooling transition was set to -44.5 ± 0.5MHz and the dispenser current was 7.0 ± 0.1A.

Chapter 5

Mirror MOT in the Science Chamber

5.1 Realisation of Mirror MOT

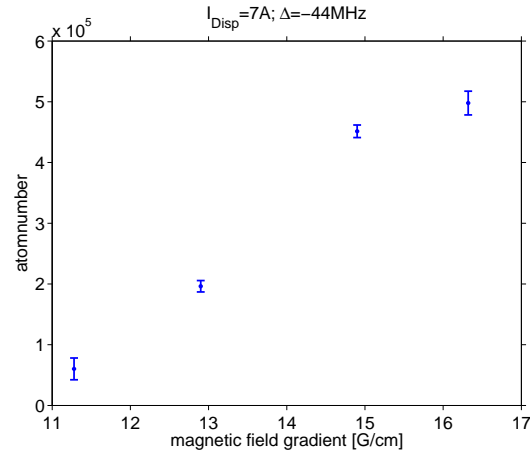A mirror MOT of ^{87}Rb was realised, loading a (very) small number of atoms from the background vapour. A current of 61A was passed through the copper U structer and horizontal and vertical bias fields were 11.34 ± 0.04G and 4.67 ± 0.05G, respectively, upon this realisation.

5.2 The push beam and realisation of Loading from Collection MOT to Mirror MOT

The loading of atoms from the collection MOT into the mirror MOT via the push beam was realised. Currently, the Mirror MOT is still under optimization. Up to now (05/08/08) we have been able to trap slightly more than 10^7 ^{87}Rb atoms and we intend to increase this number further to the order of 10^9 atoms (there are 17 parameters to vary, not all of which are independent). Due to the fact that the experiment is, at the moment, not running in a sufficiently stable manner to derive highly reproduceable results, all results in this section should be regarded as preliminary.

The degrees of freedom in the alignment and setup of the push beam are numerous. The available parameters are:

- push beam intensity

- push beam frequency

- polarization of the push beam

- diameter of the push

- position of the collection MOT relative to the axis of the push beam

- position of the science MOT relative to the chip surface and the axis of the push beam

Due to this huge parameter space, in combination with the parameters[1] for the operation of the science MOT, it took time to first establish the science MOT.

Fig. 5.1 illustrates the loading behaviour of the Collection MOT with and without push beam action. It can clearly be seen that, due to the push beam interaction, the collection MOT is operating at approximatly 10% of its original value, thereby acting as an atom source for the science MOT.
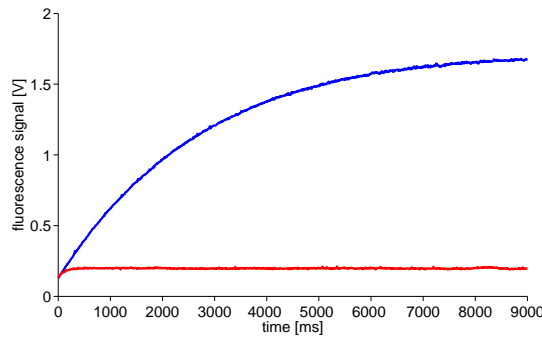
Figure 5.1: Collection MOT fluorescence signal with (red) and without (blue) push beam. Due to the push beam interaction, the collection MOT is operating at approximatly 10% of its original value, thereby being acting as an atom source for the science MOT.

In our setup, the optimal value of the push beam intensity (on resonance) was found to be 350μW [2] (see Fig. 5.2). The push beam emanating from the fibre was centred with an aperture approximately 1mm in diameter, after which the power was measured.

---

[1] frequency and polarization of trapping beams, beam alignment, quadrupole magnetic field, for both collection and mirror MOTs

[2] resonant with the $F = 2 \rightarrow F' = 3$ transition of the ^{87}Rb D_2-line

Figure 5.2: Science MOT photodiode signal against to push beam power

This data was taken during iteratively optimizing the science mirror MOT. A maximum in the fluorescence signal, detected with a pho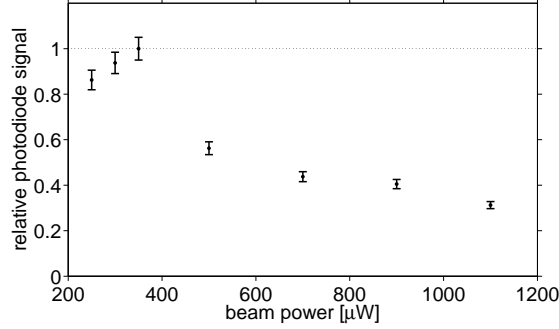todiode, was found to be at a push beam intensity of 350μW. Data plotted relative to the maximum value. $I_U = 60$A, $I_{bias}^{horizontal} = 3.3$A, $I_{bias}^{vertical} = 2.9$A.

In the case of the detuning of the push beam, a local maximum was found at $\Delta_{peak} = +2\pi \times 16$MHz, as illustrated in Fig. 5.3. However, this is a local maximum for the push beam power. It is likely that there are many local maxima, some larger than others, as found by other research groups [66].
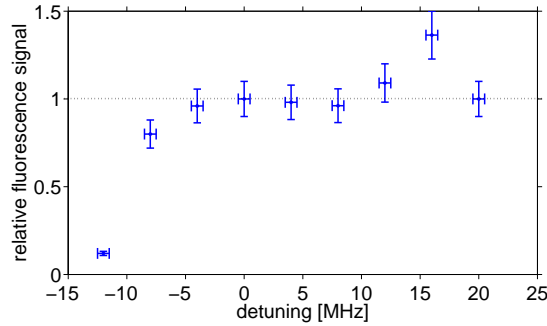
Figure 5.3: Dependence of science MOT fluorescence signal on the detuning of the push beam

The fluorescence signal is plotted relative to its value at to zero detuning. A second peak is found for a blue detuning of 16MHz. $I_U = 60$A, $I_{bias}^{horizontal} = 3.3$A, $I_{bias}^{vertical} = 2.9$A.

The whole parameter space of the push beam frequency and detuning is yet to be explored. This parameter space is complicated by the choice of push beam polarisation, the position of the collection MOT with respect to the push beam, and the magnetic field gradient of the

collection MOT. The installation of a lens, focusing the push beam on the collection MOT, is still in debate. However, experiences by other experiments of our group have not been satisfactory.

5.3 Lifetime of the Rubidium Mirror MOT

The collection MOT is loaded directly from background vapour pressure (see section 4.2.3), whereas the science MOT is only loaded via the push beam. By switching off the push beam, the science MOT loss processes (see section 4.2.3) are not compensated anymore by the reloading through the push beam. Therefore, the number of trapped atoms (and the resulting fluorescence signal) decays, as can be seen in Fig. 5.4. An non-linear least-squares fit using the Levenberg-Marquard algorithm delivers a decay time[3] of 19 ± 1s.
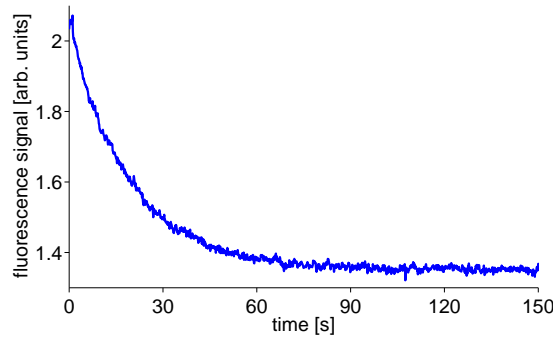

Figure 5.4: Mirror MOT decay after blocking push beam

5.4 Upcoming Optimisation

5.4.1 The many Parameters

The optimisation will be a difficult task because many of the variables are not independent. The variables are:

---

[3]time at which signal has decreased to $1/e$ of its initial value

- push beam frequency, intensity, polarization, beam diameter, spatial orientation and overlap with the collection and mirror MOTs.

- collection MOT position and loading rate, depending on cooling and repumping beam frequency, intensity, polarization, gradient of the magnetic field, beam alignment and finally the current of the atom dispensers

- mirror MOT position and loading rate, depending on the push beam action, and furthermore, on the frequency, intensity, polarization of cooling and repumping beams, beam alignment and the gradient of the magnetic field.

5.4.2 Immediate Action

- increase the loading rate of collection MOT, to increase number of atoms per second available for transfer (atom flux to mirror MOT). This is an important step from this point onwards.

- optimise the power and detuning of push beam for maximum atom loss in the collection MOT, without having the push beam power or detuning set such that it is deleterious to the mirror MOT

- optimise the beam alignment of mirror MOT

- optimise the detuning and intensity for mirror MOT

- optimise the push beam orientation

- optimise the position of collection MOT relative to push beam

Chapter 6

Conclusions

During this diploma work, the bias coils were characterised, the collection chamber and the home-built potassium dispensers were tested by creating a single ^{87}Rb and a single ^{40}K MOT, and the vacuum problems of the science chamber were dealt with. The atom chip was installed into the science chamber and the collection the science chambers were succesfully connected. The optical setups for both MOTs were installed, the collection MOT was again realised and finally a mirror MOT was given life to. We are currently looking forward to making the experimental setup work in a sufficiently stable manner and, subsequently, find the optimal parameters for the mirror MOT. Finally, we want to achieve a stable and reproducible ^{87}Rb BEC to subsequently sympathetically cool ^{40}K atoms and generate a degenerate Bose-Fermi mixture. From this point we will proceed to investigate the dynamics and properties of Bose-Fermi mixtures, particularly in the effectively one-dimensional regime.

Appendix A

^{40}K and ^{87}Rb D_2-line Data

	symbol	^{40}K	^{87}Rb
Atomic Number	Z	19	37
Relative Natural Abundance	μ	0.0117(1)% [37]	27.83(2)% [15]
Atomic Mass	m	39.9639987(3)u [67]	86.909180520(20) [15]
Nuclear Lifetime	$t_{1/2}$	$1.277 \cdot 10^9$a [68]	$4.88 \cdot 10^{10}$a [15]
Wavelength (Vacuum)	λ	766.701nm [69]	780.241nm [15]
Wavelength (Air)	λ_{air}	766.4911nm [69]	780.03200nm [15]
Saturation Intensity	I_S	1.796mW/cm² [16, 65]	1.669(2)mW/cm² [15]
Lifetime of the excited state	τ	25.7ns [16]	26.24(4)ns [15]
Natural Line Width (FWHM)	Γ	$2\pi \cdot 6.2$MHz [16]	$2\pi \cdot 6.065(9)$MHz [15]
Recoil Velocity	v_{rec}	1.302cm/s [16]	0.588cm/s [15]
Recoil Temperature	T_{rec}	815nK [16]	362nK [15]
Doppler Temperature	T_D	149μK [16]	146μK [15]

Table A.1: ^{40}K and ^{87}Rb D_2-line data

Note:

- I_s =saturation intensity of the following D_2 transitions for $\sigma^\pm$ polarized light:

    ^{40}K : $\left|4^2S_{1/2}, F = 9/2, m_F = \pm 9/2\right\rangle \longleftrightarrow \left|4^2P_{3/2}, F = 11/2, m_F = \pm 11/2\right\rangle$

    ^{87}Rb : $\left|5^2S_{1/2}, F = 2, m_F = \pm 2\right\rangle \longleftrightarrow \left|5^2P_{3/2}, F = 3, m_F = \pm 3\right\rangle$

For circularly polarized light I_s is defined as [15]

$$I_s = \frac{\hbar\omega^3\Gamma}{12\pi c^2} = \frac{\pi hc\Gamma}{3\lambda^3}. \tag{A.1}$$

τ =lifetime of the relevant exited $P_{3/2}$-level
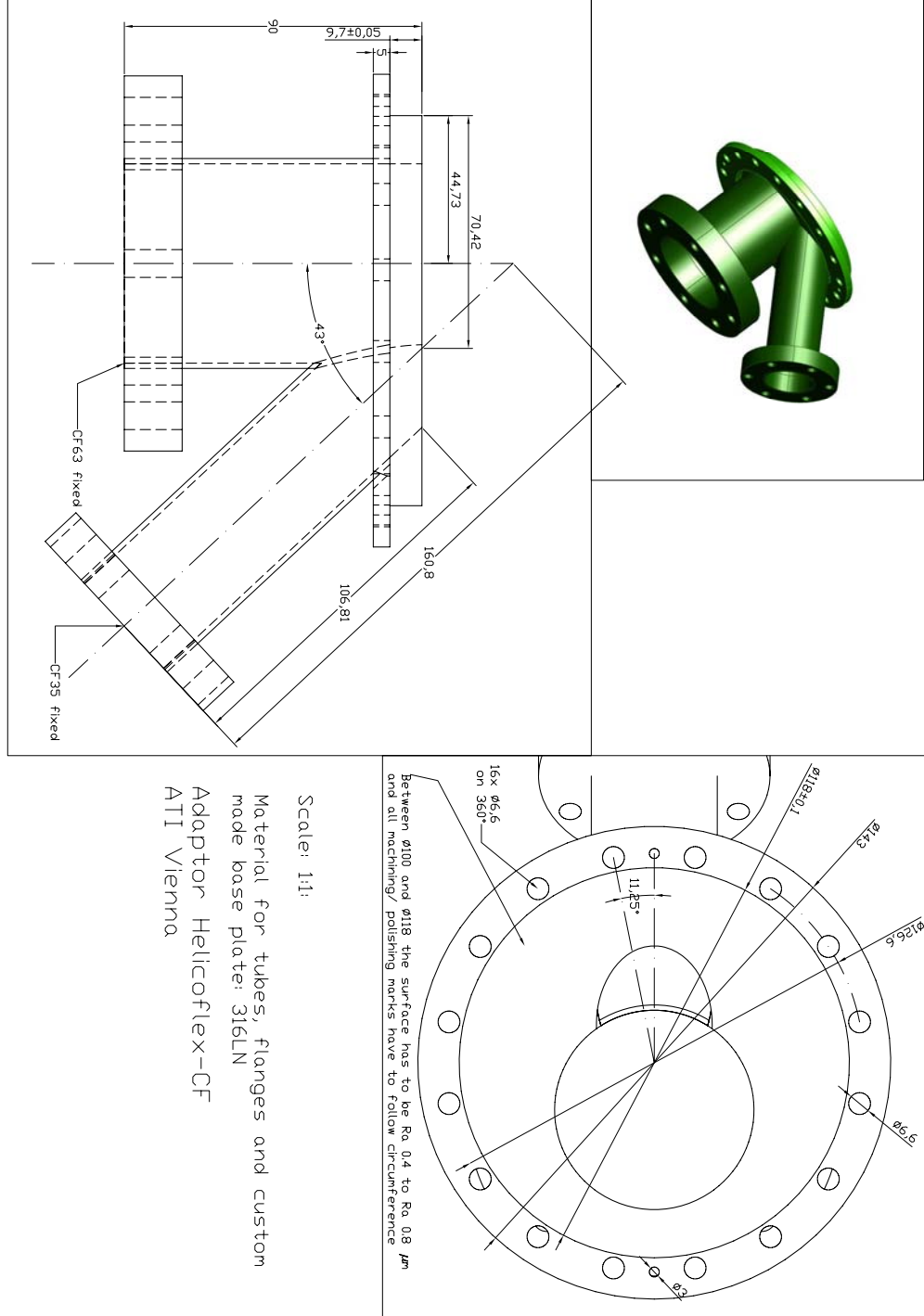
Appendix B

Window Adaptor

Figure B.1: Large window adaptor tube

In fact, two tubes are needed: one for the horizontal imaging beam and one for the 45° MOT beam. The DN35CF tube is used for the 45° MOT beam having an angle of 43° with the horizontal DN63CF. tube, due to the fact that the large windows are tilted 2° from the vertical axis. Established in collaboration with [44].

Bibliography

[1] S. BOSE, *Z. Phys.* **26**, 178 (1924).

[2] A. EINSTEIN, *Sitzungsbericht der Königlich-Preussischen Akademie der Wissenschaft* **Zweite Abhandlung** (1925).

[3] M. ANDERSON, J. E. A. WIEMAN, and E. CORNELL, *Science* **269**, 198 (1995).

[4] B. DEMARCO and D. JIN, *Science* **285**, 1703 (1999).

[5] A. G. TRUSCOTT, K. E. STRECKER, W. I. MCALEXANDER, G. B. PARTRIDGE, and R. G. HULET, *Science* **291**, 2570 (2001).

[6] M. HOLLAND, B. DEMARCO, and D. JIN, *Phys. Rev. A* **61**, 053610 (2000).

[7] L. SPITZER, *Interscience Publishers, Inc., New York* **2nd ed.**, 131 (1962).

[8] T. HÄNSCH and A. L. SCHAWLOW, *Opt. Commun.* **13**, 68 (1975).

[9] D. WINELAND and H. DEHMELT, *Bull. Am. Phys. Soc.* **20**, 637 (1975).

[10] C. J. FOOT, *Atomic Physics*, Oxford Master Series in Atomic, Optical and Laser Physics, 2005.

[11] C. COHEN-TANNOUDJI, J. DUPONT-ROC, and G. GRYNBERG, *Atom-Photon Interactions*, Wiley-VCH, 1998.

[12] H. J. METCALF and P. V. DER STRATEN, *Laser Cooling and Trapping*, Springer, 1999.

[13] W. DEMTRÖDER, *Laser Spectroscopy*, Springer-Verlag GmbH, 2002.

[14] S. Chu, L. Hollerberg, J. B. A. Cable, and A. Ashkin, *Phys. Rev. Lett.* **55**, 48 (1985).

[15] D. A. Steck, Rubidium 87 D Line Data, available online at: http://steck.us/alkalidata/ (accessed 01.08.2007....), 2001, Los Alamos National Laboratory.

[16] F. Henkel, Fermionisches Kalium in der Dreikomponentigen Magnetooptischen Falle, Master's thesis, Ludwig-Maximilians-Universität München, 2005.

[17] P. Lett, R. Watts, C. Westbrook, W. Phillips, P. Gould, and H. Metcalf, *Phys. Rev. Lett.* **61**, 169 (1988).

[18] J. Dalibard and C. Cohen-Tannoudji, *J. Opt. Soc. Am. B* **6**, 2023 (1989).

[19] P. J. Ungar, D. S. Weiss, E. Riis, and S. Chu, *J. Opt. Soc. Am. B* **6**, 2058 (1989).

[20] M. Kasevich and S. Chu, *Phys. Rev. Lett.* **69**, 1741 (1992).

[21] D. A. Smith, *Single-Impulse Magnetic Focusing of Launched Cold Atoms*, PhD thesis, University of Durham, UK, 2005.

[22] E. Raab, M. Prentiss, A. Cable, S. Chu, and D. Pritchard, *Phys. Rev. Lett.* **59**, 2631 (1987).

[23] C. G. vom Hagen, *Towards a low-dimensional degenerate Fermi-Fermi-Bose mixture*, PhD thesis, Ruperto-Carola University of Heidelberg, Germany, 2008.

[24] P. C. D. Hobbs, *Building Electro-Optical Systems: Making It All Work*, John Wiley, 2000.

[25] H. J. Dirschmid, W. Kummer, and M. Schweda, *Einführung in die mathematischen Methoden der Theoretischen Physik*, Vieweg, 1976.

[26] J. M. Supplee, E. A. Whittake, and W. Lenth, *Appl. Opt.* **33**, 6294 (1194).

[27] L. Ricci, M. Weidemüller, T. Esslinger, A. Hemmerich, C. Z. A. Vuletic, W. König, and T. W. Hänsch, *Opt. Commun.* **117**, 541 (1995).

[28] C. E. WIEMAN and L. HOLLBERG, *Rev. Sci. Instrum.* **62(1)**, 1 (1991).

[29] D. MESCHEDE, *Optik, Licht und Laser*, Teubner, 1999.

[30] G. FISCHER, *J. Opt. Commun.* **8**, 18 (1987).

[31] C. KITTEL, *Einführung in die Festkörperphysik*, Oldenburg Verlag, 12 edition, 1999.

[32] P. HOROWITZ and W. HILL, *The art of electronics*, Cambridge University Press, 1989.

[33] S. R. SYSTEMS, About Lock-In Amplifers, Application Note 3, Technical report, Stanford Research Systems, 2008.

[34] M. L. HARRIS, C. S. ADAMS, S. L. CORNISH, I. C. M. LEAD, E. TARLETON, and I. G. HUGHES, *preprint, arXiv*, 0509157 v2 (2006).

[35] C. P. PEARMAN, C. S. A. ADN S. G. COX, D. A. SMITH, and I. G. HUGHES, *J. Phys. B: At. Mol. Opt. Phys.* **35**, 5141 (2002).

[36] J. M. REEVES, O. GARCIA, and C. A. SACKETT, *Applied Optics* **45**, 372 (2006).

[37] Isotopic Compositions of the Elements 1989, Commission on Atomic Weights and Isotopic Abundances Report for the International Union of Pure and Applied Chemistry, 1989.

[38] W. SCHÜNEMANN, H. ENGLER, R. GRIMM, M. WEIDEMÜLLER, and M. ZIELONKOWSKI, *Review of Scientific Instruments* **70(1)**, 242 (1999).

[39] B. SHIRINZADEH and C. C. WANG, *Appl. Opt.* **22**, 3265 (1983).

[40] S. SCHNEIDER, *Bose-Einstein Kondensation in einer magnetischen Z-Falle*, PhD thesis, Ruprecht-Karls-Universität Heidelberg, Germany, 2003.

[41] S. WILDERMUTH, P. KRÜGER, C. BECKER, M. BRAJDIC, S. HAUPT, A. KASPER, R. FOLMAN, and J. SCHMIEDMAYER, *Phys. Rev. A* **69**, 030901 (2004).

[42] S. WILDERMUTH, *Neue Experimente mit Atomchips*, PhD thesis, Universität Heidelberg, 2002.

[43] J. FORTÁGH and C. ZIMMERMANN, *Rev. Mod. Phys.* **79**, 235 (2007).

[44] M. GÖBEL, *N.N.*, PhD thesis, Universität Heidelberg, 2008.

[45] WUTZ, *Handbuch Vakuumtechnik*, vieweg, 2006.

[46] J. F. O'HANLON, *A User's Guide to Vacuum Technology*, Wiley, 2003.

[47] J. REICHEL, W. HÄNSEL, and T. W. HÄNSCH, *Phys. Rev. Lett.* **83(17)**, 3398 (1999).

[48] R. FOLMAN, P. KRÜGER, D. CASSETTARI, B. HESSMO, T. MAIER, and J. SCHMIED-MAYER, *Phys. Rev. Lett.* **84(20)**, 4749 (2000).

[49] R. FOLMAN, P. KRÜGER, J. SCHMIEDMAYER, J. DENSCHLAG, and C. HENKEL, *Advances in Atomic, Molecular, and Optical Physics* **48** (2002).

[50] W. KETTERLE, D. S. DURFREE, and D. M. STAMPER-KURN., *Academic Press*, 1 (1998).

[51] A. ARNOLD, *Preparation and Manipulation of an ^{87}Rb Bose-Einstein Condensate*, PhD thesis, University of Sussex UK, 1999.

[52] M. BARTENSTEIN, Aufbau und Charakterisierung einer kontinuierlich betriebenen Doppel-MOT für ^{87}Rb, Master's thesis, Universität Innsbruck/Freie Universität Berlin, 2001.

[53] M. WILZBACH, Aufbau eines Experiments zur miniaturisierten und integrierten Detektion neutraler Atome, Master's thesis, Universitaet Heidelberg, 2002.

[54] B. ANDERSON and M. A. KASEVICH, *Phys. Rev. A* **63**, 23404 (2001).

[55] K. LEVENBERG, *The Quarterly of Applied Mathematics* **2**, 164 (1944).

[56] D. MARQUARDT, *SIAM Journal on Applied Mathematics* **11**, 431 (1963).

[57] T. SCHUMM, Auf dem Weg zu einem ^{87}Rubidium Bose-Einstein-Kondensat in magnetischen Drahtfallen, Master's thesis, Universität von Heidelberg, 2001.

[58] A. KASPER, *Bose-Einstein condensation in a robust microtrap — the combination of wire traps and atom chips*, PhD thesis, Ruperto-Carola University of Heidelberg, 2003.

[59] R. S. WILLIAMSON, *Magneto-Optical Trapping of Potassium Isotopes*, PhD thesis, University of Wisconsin - Madison, 1997.

[60] E. ARIMONDO, M. INGUSCIO, and P. VIOLINO, *Rev. Mod. Phys.* **49**, 31 (1977).

[61] J. CATANI, P. MAIOLI, L. D. SARLO, F. MINARDI, and M. INGUSCIO, *Phys. Rev. A* **73**, 033415 (2006).

[62] J. CATANI, A New Apparatus for ultracold K-RB Bose-Bose Atomic Mixtures, Master's thesis, Università degli studi di Firenze, 2006.

[63] K. LINDQUIST, M. STEPHENS, and C. WIEMAN, *Phys. Rev. A* , 4082 (1992).

[64] K. E. GIBBLE, S. KASAPI, and S. CHU., *Optics Letters* **17**, 526 (1992).

[65] M. TAGLIEBER, A.-C. VOIGT, F. HENKEL, S. FRAY, T. W. HÄNSCH, and K. DIECKMANN, *Phys. Rev. A* **73**, 011402 (2006).

[66] K. BONGS, Private communication concerning push beam experiments in the group of K. Sengstock, Hamburg, 2008.

[67] I. MILLS, T. CVITAS, K. HOMANN, N. KALLAY, and K. KUCHITSU, *Blackwell Scientific Publications* (1988).

[68] R. R. KINSEY, *paper submitted to the 9th International Symposium of Capture Gammaray Spectroscopy and Related Topics, Budapest, Hungary* , Data extracted from NUDAT database (Jan. 14/1999) (October 1996).

[69] NIST Atomic Spectra Database Lines Data, available online at: http://physics.nist.gov/PhysRefData/ASD/lines_form.html, accessed 03.09.2007.